Upper-Ocean Inertial Currents Forced by a Strong Storm. Part I: Data and Comparisons with Linear Theory*

ERIC A. D'ASARO,** CHARLES C. ERIKSEN,† MURRAY D. LEVINE,‡
PETER NIILER,§ CLAYTON A. PAULSON,‡ AND PIM VAN MEURS§

** *Applied Physics Laboratory, College of Ocean and Fishery Sciences, University of Washington, Seattle, Washington*
† *University of Washington, Seattle, Washington*
‡ *Oregon State University, Corvallis, Oregon*
§ *Scripps Institution of Oceanography, La Jolla, California*

(Manuscript received 25 April 1994, in final form 20 January 1995)

ABSTRACT

A strong, isolated October storm generated 0.35–0.7 m s^{-1} inertial frequency currents in the 40-m deep mixed layer of a 300 km × 300 km region of the northeast Pacific Ocean. The authors describe the evolution of these currents and the background flow in which they evolve for nearly a month following the storm. Instruments included CTD profilers, 36 surface drifters, an array of 7 moorings, and air-deployed velocity profilers. The authors then test whether the theory of linear internal waves propagating in a homogeneous ocean can explain the observed evolution of the inertial frequency currents.

The subinertial frequency flow is weak, with typical currents of 5 cm s^{-1}, and steady over the period of interest. The storm generates inertial frequency currents in and somewhat below the mixed layer with a horizontal scale much larger than the Rossby radius of deformation, reflecting the large-scale and rapid translation speed of the storm. This scale is too large for significant linear propagation of the inertial currents to occur. It steadily decreases owing to the latitudinal variation in f, that is, β, until after about 10 days it becomes sufficiently small for wave propagation to occur. Inertial energy then spreads downward from the mixed layer, decreasing the mixed layer inertial energy and increasing the inertial energy below the mixed layer. A strong maximum in inertial energy is formed at 100 m ("the Beam"). By 21 days after the storm, both mixed layer inertial energy and inertial frequency shear maximum just below the mixed layer have been reduced to background levels. The total depth-average inertial energy decreases by about 40% during this period.

Linear internal wave theory can only partially explain the observed evolution of the inertial frequency currents. The decrease in horizontal wavelength is accurately predicted as due to the β effect. The decrease in depth-average inertial energy is explained by southward propagation of the lowest few modes. The superinertial frequency and clockwise rotation of phase with depth are qualitatively consistent with linear theory. However, linear theory underpredicts the initial rate at which inertial energy is lost from the mixed layer by 20%–50% and cannot explain the decrease of mixed layer energy and shear to background levels in 21 days.

1. Introduction

The famous equations of Ekman (1905) describe how a homogeneous ocean responds to the wind, producing both a current proportional to the wind stress and velocities that oscillate at the local inertial frequency. Both responses are commonly found within the nearly homogeneous mixed layer of the upper ocean. The first component is described, for example, by Price et al. (1986), Davis et al. (1981), and Price et al. (1989). The inertial frequency component, which we will call inertial currents or inertial motions, is described by Webster (1968), Pollard and Millard (1970), Pollard (1980), Price (1981), and many others. Usually, these motions are nearly uniform across the mixed layer, reflecting rapid mixing within the mixed layer. This often produces a strong shear across the mixed layer base, which plays a key role in determining the downward entrainment rate of the mixed layer. Strong storms commonly produce energetic inertial currents in the mixed layer.

A simple, but very useful, model assumes that the mixed layer velocity is vertically uniform and that the ocean is horizontally homogeneous. Under these assumptions Pollard and Millard (1970) write the momentum budget of the mixed layer as

$$\frac{dU}{dt} + ifU = T - rU, \tag{1}$$

* University of Washington School of Oceanography Contribution Number 2129.

Corresponding author address: Dr. Eric A. D'Asaro, Applied Physics Laboratory, University of Washington, 1013 N.E. 40th Street, Seattle, WA 98105.
E-mail: dasaro@apl.washington.edu

where the horizontal current components (u, v) are represented by the complex number $U = u + iv$ and the wind stress components (τ_x, τ_y) by $T = (\tau_x + i\tau_y)/\rho H$. The mixed layer depth is H and its density ρ. With $r = 0$, this is Ekman's model with the eddy diffusivity infinite within the mixed layer and zero elsewhere. The steady Ekman layer has a velocity $U_E = T/(if\rho H)$. Such a model, however, cannot account for the observed decay of the inertial currents in the absence of continued forcing. Accordingly, Pollard and Millard (1970) added the empirical "decay parameter" r. The resulting model, (1), often makes good predictions of mixed layer inertial currents (Pollard 1980; Thomson and Huggett 1981; Paduan et al. 1989) provided that an appropriate mixed layer depth is used. The decay parameter is not constant, but typically has inverse values in the range of 4 to 20 days. A major goal of this paper is to understand the physics associated with this decay.

Many investigators, starting with Pollard (1970), have proposed that mixed layer inertial currents decay by propagating into the thermocline and deep ocean as near-inertial frequency internal waves. Considerable evidence supports this idea. Observations of near-inertial motions below the mixed layer usually are consistent with dominantly downward propagating waves (Leaman 1976; D'Asaro and Perkins 1984; Müller et al. 1983) carrying a vertical energy flux comparable to the flux of energy from the wind to mixed layer inertial motions (D'Asaro and Perkins 1984; D'Asaro 1985; Käse 1979). Observations of near-inertial motions associated with both midlatitude storms (Kundu and Thomson 1985) and, in particular, hurricanes (Price 1983; Sanford et al. 1987) commonly show the expected increase in thermocline near-inertial motions and many of the structural features expected for linear propagation.

Dynamics other than wave propagation has also been proposed to explain the decay factor in (1). Bell (1978) suggests that high-frequency internal waves generated at the base of the mixed layer can transport its inertial frequency momentum into the thermocline. Kroll (1982) proposes a viscous instability of the mixed layer. Others (Smith 1973), despairing that linear dynamics could be made to account for real observations, have concluded that the wind itself is the major agent for both generating and dissipating inertial currents.

The background mesoscale eddy field can also change inertial frequency currents in ways not described by (1). Kunze (1985), for example, shows that mesoscale vorticity ζ acts to shift the Coriolis frequency for near-inertial frequency internal waves from f to approximately $f_{\text{eff}} = f + \frac{1}{2}\zeta$. Subinertial frequency currents can also advect and strain inertial currents.

It has become common to refer to near-inertial frequency motions in the ocean as near-inertial frequency "waves," thus implicitly accepting that wave dynamics controls their evolution. The main goal of our paper is to test this hypothesis.

The Ocean Storms Experiment was conducted during the fall, winter, and spring of 1987/88 in order to address these and other issues related to upper-ocean dynamics. The site was selected for the combination of strong wind forcing and a weak mesoscale eddy field, so that advective effects would be minimized. The observed velocity data are dominated by energetic inertial motions generated by a small number of storms. The paper by Levine and Zervakis (1995) in this volume shows the entire velocity record and analyzes all of the major inertial current generation events. The one best documented was a storm that passed over the experimental site on 4 October 1987 and was followed by nearly a month of weak winds. The storm produced strong inertial currents, whose evolution could be followed for a month afterward. Furthermore, the sampling of this event was very good since an array of surface drifters was deployed in early October. The combination of strong inertial motions generated by a single storm, three-dimensional sampling, and a long period of observation make this event nearly ideal for studying the evolution of storm-generated inertial motions. The data are sufficiently detailed not only to describe the evolution of the inertial motions in the context of linear internal wave theory but also to test the applicability of the theory to these data.

We analyze the evolution of inertial currents generated by this storm. The oceanographic response was sampled using a diverse set of instrumentation. High-resolution sampling in depth and time was achieved using a 7-element moored array concentrated in the upper 100 m of the ocean but with one line of current meters extending over the full ocean depth; high-resolution sampling in the horizontal and time was obtained using a 36-element surface drifter array, and high-resolution in three dimensions was achieved using surveys of air-deployed expendable velocity profilers. These data resolve the horizontal and vertical structure of the inertial currents for nearly a month after the storm over a region several hundred kilometers square.

Owing to the complexity of the data and analysis, our work is presented in several parts. Part I, this paper, describes the subinertial and inertial frequency currents and makes simple comparisons between the observations and linear theory. Part II (D'Asaro 1995a) compares these observations in detail with a nonlinear numerical simulation of flow. Part III (D'Asaro 1995b) analyzes the interaction of the mixed layer inertial currents and the background mesoscale flow.

Many of the other papers in this volume contain complementary information. Crawford and Large (1995) and Large and Crawford (1995) describe the wind field, the associated generation of the mixed layer inertial currents, and the resulting upper-ocean mixing. Levine and Zervakis (1995), Zervakis and Levine (1995), and Qui et al. (1995) use a subset of the data

presented here to test the dynamics of the inertial motions. Matear (1993) has described the low-frequency motion. Paduan and Niiler (1993) have described the mixed layer low-frequency motions and the mixed layer heat budget.

2. Linear wave theory

We consider the inviscid, linear response of a horizontally uniform, flat-bottomed ocean following Gill (1984) and D'Asaro (1989). A storm accelerates inertial currents in the mixed layer in a time that is short compared with the near-inertial frequency wave propagation time, so that at time $t = 0$, the horizontal velocity is $U(x, y, t)Z(z)$. For times $t > 0$ the wind stress is zero.

Gill (1984), Kundu and Thomson (1985), and Eriksen (1988) show that the barotropic response to a fast moving storm is weak, so we consider only the baroclinic, near-inertial frequency response. The initial velocity profile is expanded in terms of the hydrostatic baroclinic modes of the stratification, $p_n(z)$:

$$Z(z) = \sum_{n=1}^{\infty} \sigma_n p_n(z), \tag{2}$$

where $p_n(z)$ is the eigenfunction of the nth mode and σ_n is the projection of $Z(z)$ onto the nth mode. The solution to the linear equations is also written as a sum of modes,

$$U(x, y, z, t) = \sum_{n=1}^{\infty} \tilde{U}_{In}(x, y, t)p_n(z)e^{-if_0t}, \tag{3}$$

where the velocity is represented as a complex number as in (1), $\tilde{U}_I$ is the amplitude of the inertial component of mode n, and f_0 is the inertial frequency at a reference latitude. Smith (1973) and D'Asaro (1989) analyze the linear equations of motion under the assumption that U_{In} varies slowly compared with f^{-1} and find a simplified equation that governs its evolution:

$$\frac{\partial \tilde{U}_{In}}{\partial t} = i\frac{c_n^2}{2f_0}\nabla_H^2\tilde{U}_{In} + i(f(y) - f_0)\tilde{U}_{In}. \tag{4}$$

Here the Coriolis frequency $f(y)$ varies as a function of north–south distance y. Equation (4) filters high-frequency gravity waves from the equations of motion. On an f plane, or locally in a WKB sense, (4) produces the familiar dispersion relationship for near-inertial motions:

$$\omega_n - f = \frac{c_n^2}{2f}\alpha^2, \tag{5}$$

where ω_n is the frequency, c_n is the modal phase speed, and $\alpha^2 = k^2 + l^2$, where k and l are the east and north horizontal wavenumber components.

The initial stages of wave propagation can intuitively be described by "inertial pumping" (Price 1983; Gill 1984; D'Asaro 1989). The divergence of the inertially oscillating mixed layer currents produces an oscillating vertical displacement of the mixed layer base. This results in oscillating pressure gradients in the thermocline and accelerates inertial currents at depth. The rate of energy transfer depends on the horizontal scale of the mixed layer inertial currents, as expressed by the ∇_H^2 term in (4). Small-scale inertial currents propagate more rapidly than large-scale inertial currents.

Mathematically, it is more convenient to describe the evolution of the mixed layer inertial currents using the normal mode expansion (3). Gill (1984) derives a simple expression for the rate of decay of mixed layer inertial currents. He considers the case in which the mixed layer inertial currents at $t = 0$ vary sinusoidally:

$$\tilde{U}_I(x, y, 0) = \tilde{U}_0 e^{i(kx+ly)}. \tag{6}$$

The modal amplitudes are

$$\tilde{U}_{In}(x, y, 0) = \sigma_n\tilde{U}_0 e^{i(kx+ly)}. \tag{7}$$

Each mode has a different frequency given by (5), so its phase relative to a pure inertial rotation is

$$\theta_n(t) = \frac{c_n^2}{2f}\alpha^2 t. \tag{8}$$

Since c_n decreases with n, the low modes have the highest frequency and rotate fastest. Gill (1984) defines times

$$t_n = \pi\frac{f_0}{\alpha^2 c_n^2} \tag{9}$$

for which $\theta_n = \frac{1}{2}\pi$. At time t_1, the first mode has rotated 90° and the amplitude of the mixed layer inertial current is reduced from U_0 to $(1 - \sigma_1)U_0$. The horizontal group speed of the nth mode is

$$G_H = c_n^2\frac{\alpha}{f}. \tag{10}$$

At time t_n the mode has propagated a distance

$$\Delta = \frac{\pi}{\alpha}, \tag{11}$$

or one-half wavelength.

The net effect is a vertical spreading of energy from the mixed layer due to growing incoherence between the modes and a horizontal spreading of total water column energy due to propagation. For horizontally uniform inertial currents, the modes will rotate back into phase at later times; this occurs at time $2t_1$ for the first mode. However, Gill (1984) shows that the mixed layer usually does not regain its initial amplitude, as additional higher modes have usually rotated out of phase by this time. For inertial currents, generated in a confined region comparable in size to the wavelength, the amplitude of mode n will be significantly reduced by time $2t_n$ owing to horizontal propagation, and the

effects of rephasing will be small. Gill (1984) provides a simple recipe for approximating the average rate of energy loss from the mixed layer: at time t_1 the effect of mode 1 disappears from the mixed layer and the mixed layer velocity decreases to a fraction $1 - \sigma_1$ of its initial value. Similarly, at time t_2 the amplitude decreases to $1 - \sigma_1 - \sigma_2$, and so on.

Mixed layer inertial currents are not generally sinusoidal as assumed above. Below, we will generalize these relationships to allow direct comparison of the above theory with our data. The inertial currents also interact with subinertial currents. This is discussed in Parts II and III.

3. Data

a. CTD profiles

A grid of 34 CTD stations was made at the Ocean Storms site from 30 September to 7 October from the CRV *Parizeau*. Measurements were made with a Guildline 8705 CTD, calibrated by water samples (Tabata et al. 1988). Most stations were to a depth of nearly 1500 dbars. The CTD salinity was corrected using water samples and occasional full hydrocasts analyzed on board. Differences between the calibrated CTD data and the hydrocast data ranged from less than 0.005 psu to 0.02 psu (1 psu = 1‰). An error of 0.01 psu, if constant with depth, is equivalent to about 0.006 surface dynamic meters referenced to 800 dbars, which is negligible.

b. Near-surface drifters

An array of Argos-tracked TRISTAR drifting buoys (Paduan and Niiler 1993; Niiler et al. 1987) drogued at 15 m were deployed starting on day 275 of 1987. A total of 15 were operational by the beginning of the storm on day 277 (4 October). The array grew to 36 drifters by day 282 and contained 35 on day 295.

Niiler and Paduan (1995) describe a model in which these drifters slip downwind relative to the water at 15 m at 0.1% of the 10-m wind speed for moderate and low wind speeds. During the period of interest here, days 278–300 of 1987, the maximum 10-m measured wind speed was just below 10 m s^{-1} and the vector mean wind speed was about 3 m s^{-1} (see section 3d). The maximum predicted slippage is thus 0.01 m s^{-1} and the vector average is 0.003 m s^{-1}. Almost all of the CTD profiles showed a well-mixed layer extending to about 40 m, so we expect little slippage due to shear.

Even for a perfect drifter, the velocities at 15 m should be correlated to the wind due to the presence of wind forced motions at 15 m. Niiler and Paduan (1995) correlate wind stress and drifter motion for 47 TRISTAR-II drifters including the ones used here. The drifter velocity coherent with the wind is 70° to the right of the wind with a magnitude $\tau/\rho f H_{\text{eff}}$ for wind stress τ, water density ρ, and an effective depth H_{eff} equal to about 35 m. A typical wind stress of 0.05 Pa yields a wind-forced flow of about 0.012 m s^{-1}. The vector average stress of 0.03 Pa would produce an average flow of 0.008 m s^{-1}.

The raw buoy positions obtained from System Argos were demodulated into inertial and subinertial positions and velocities using two nearly equivalent methods. The method described by D'Asaro (1992) uses smoothing splines with a smoothing parameter of $4/f$. This was used on only two drifters (Argos ID 7986, 7951). An objective analysis method, described in the appendix, was used on the remaining drifters. The two methods produce very similar results. The average difference in the demodulated inertial component of velocity is about 0.1 cm s^{-1} and the rms difference around this mean is about 2 cm s^{-1}, somewhat less than the estimated rms error in the first method (D'Asaro 1992). The rms difference between the subinertial velocity components computed by the two methods is about 0.5 cm s^{-1}, about 60% of the error in the first method as estimated by D'Asaro (1992). Spectrally, the objective analysis scheme has a slightly narrower bandwidth and thus roughly 20% less energy for periods of 1.5–4 days. D'Asaro (1992) shows that energy in this band can be aliased by the irregular Argos sampling pattern, so the difference between the two schemes is concentrated in the region of most intrinsic uncertainty.

Figure 1 shows the interpolated trajectories for all the drifters. There is clearly a strong inertial component, shown by the clockwise rotating circles, and a smaller subinertial component.

c. Moorings

The moored array is shown by the triangles in Fig. 2. A profiling current meter (PCM in Fig. 2) sampled velocity, temperature, and salinity every 10 m over approximately 40–200 m at 4-hour intervals (Eriksen et al. 1982). A subsurface mooring (OSU in Fig. 2) was instrumented with vector measuring current meters (VMCM) at 20-m intervals from 60–160 m and at 195 m, and with Aanderaa RCM-5 current meters at 500 m, 1000 m, 2000 m, 3000 m, and 4000 m. These measured currents and temperature at 15-minute (VMCM) and 1-hour (Aanderaa) intervals (Zervakis and Levine 1995).

Moorings central (C), north (N), and west (W) all contained acoustic Doppler current profilers (ADCP) looking upward from 110 m. Unfortunately, only the mixed layer data from these instruments were made available for this analysis. The deeper data will be reported elsewhere. An Argos transmitter on the surface float of each mooring was used to remove the mooring motion. Mooring velocity was computed from these data, using the objective analysis scheme described in the appendix, and added to the ADCP velocity to form the oceanic velocity. The estimated mooring motion

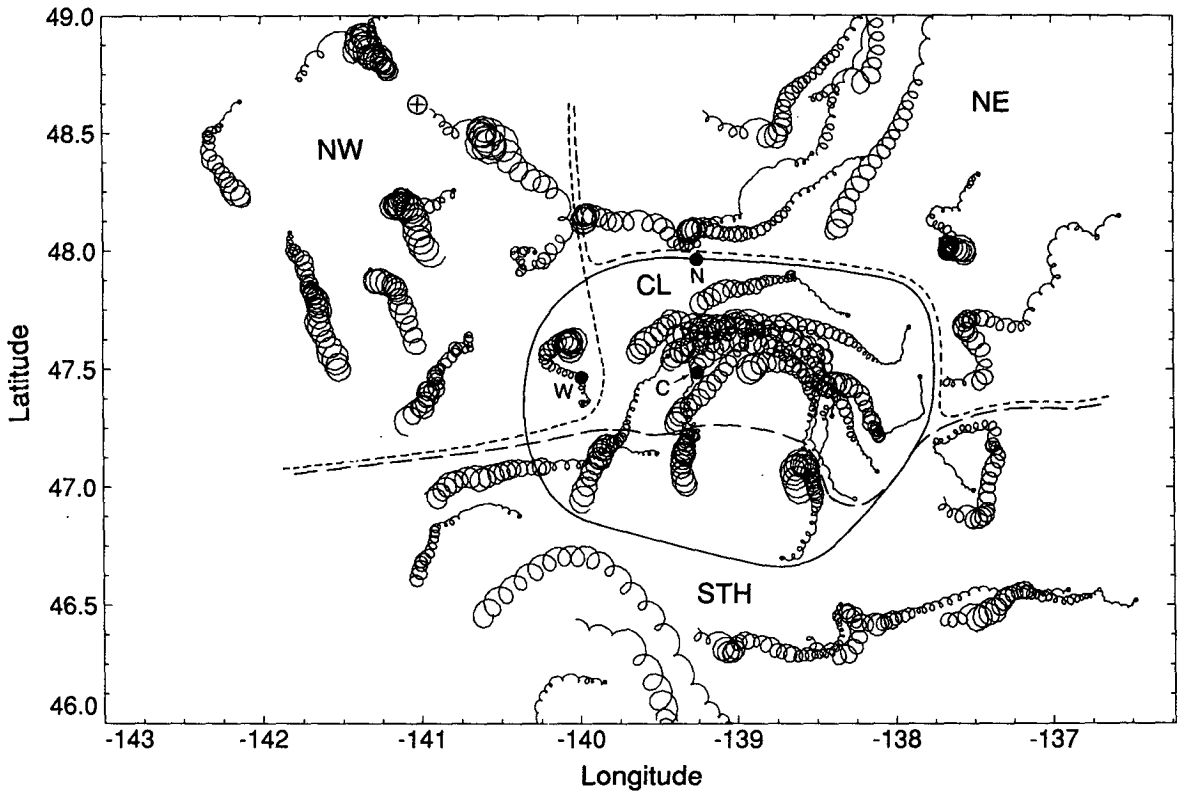

FIG. 1. Mixed layer drifter trajectories for days 275–300 of 1987 interpolated and filtered as described in the text. Many drifters were not deployed until day 280. Moorings (N, W, C) are indicated by the three large dots. The light lines define the geographic subregions used in the analysis: NE, NW (small dashes); CL (solid line); and STH (long dashes). The large circled "+" indicates a sample drifter discussed in the text.

was 0.036 m s^{-1} rms with a maximum speed of 0.09 m s^{-1} during the storm. The estimated inertial component of mooring motion is coherent with estimated inertial currents in the mixed layer; a linear correlation between these explains 75% of the mooring motion energy. Both the residual from this correlation and the rms mooring motion during periods of weak winds and current suggest that the error in the estimate of mooring motion is about 0.02 m s^{-1} rms, comparable to the error in the demodulation of the Argos tracking data.

Although no measurements of mooring motion were made at either the OSU or PCM moorings, the magnitude of the motion can be bounded by simple models using the pressure measured near the top of each mooring. A mooring may move horizontally like an inverted pendulum in response to inertial currents. Given the 0.3 m rms inertial frequency pressure fluctuations of the OSU mooring, and assuming, pessimistically, a perfectly stiff, 4000-m long, mooring pivoting at the ocean floor, we estimate an rms inertial mooring speed of less than 0.5 cm s^{-1}. A mooring may also rotate in a circle, like a precessing top, in response to the clockwise rotation of inertial currents. The maximum sustained vertical descent of the OSU mooring is less than a meter. Again, assuming a 4000-m long rigid mooring implies an inertial frequency velocity of less than 1 cm s^{-1}. In fact, the buoyancy of the OSU mooring was concentrated below 200 m, while the inertial currents are mostly above this. If we assume, optimistically, that the mooring pivots at 200 m and remains motionless below, the motion of the top of the mooring is about 5 times less than estimated above.

Similarly, the PCM mooring descends a maximum of 10 m, corresponding to a maximum inertial motion of about 3 cm s^{-1}. It also has buoyancy concentrated near 200 m, so the actual motion should be less than this.

The inertial component of velocity was extracted from each moored record by backrotating the velocity vector to 0000 UTC on day 278 (5 October) at the inertial frequency corresponding to 47.5°N and averaging these vectors over three inertial periods with a half-cosine window. We thus present all inertial velocities with the oscillatory inertial motions removed, so that a velocity vector rotating at the inertial frequency corresponding to 47.5°N is represented as a constant vector. For clarity we will use the term "backrotated inertial vector." Subinertial velocities were computed using a low-pass Butterworth filter with a 0.4 cpd cutoff.

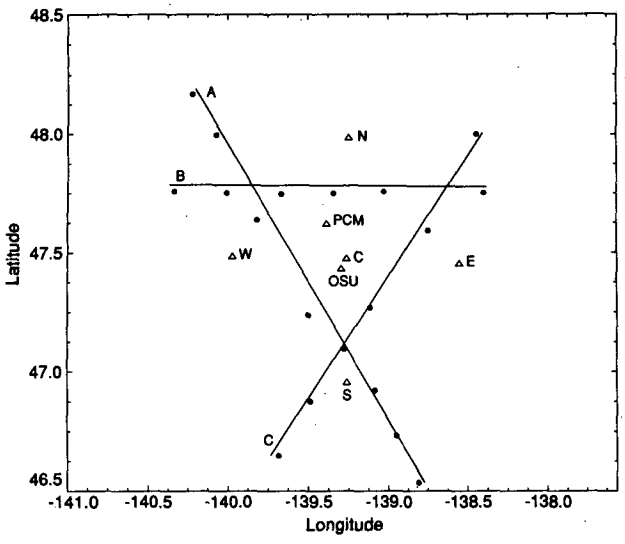

FIG. 2. Location of Ocean Storms moored array (triangles) including ADCP moorings (C, N, E, W, S), PCM mooring, and OSU mooring. The 25 October AXCP drops (filled circles) are in three sections labeled A, B, and C.

d. Wind

Wind was measured using a propeller anemometer mounted at 3-m height on the C mooring. Large et al. (1995) describe other Ocean Storms wind measurements. Wind stress was computed as in Large and Pond (1981), but with no correction for stratification since it will have minimal effect at the high wind speeds encountered here. We have several reasons to regard these stress estimates with suspicion. First, the logging system was less than ideal: 15-minute average speed and instantaneous direction every 15 minutes. Second, the drag coefficient on short timescales can vary by a factor of 2 over several hours in storms similar to ours (Large and Pond, 1981). Third, comparison with other wind data, from Large et al. (1995), suggests that these wind speeds are low at high wind speed, relative to a 10-m reference, owing to wave sheltering. They correct the winds for this effect. We will use these corrected data.

e. AXCP survey

A single survey of Sippican airborne expendable current profilers (AXCP) was made on 25 October 1987 (day 298) around the moored array (Fig. 2) using a NOAA WP-3D aircraft as described by D'Asaro et al. (1990). An AXCP measures temperature and the horizontal velocity relative to its conductivity-weighted depth average (Sanford et al. 1982). These were processed as described by Sanford et al. (1982) but with the incremental changes discussed by D'Asaro et al. (1990) and Horgan et al. (1989). The resulting relative velocity was averaged in 10 m, half overlapping bins between 15 and 1600 m and has an accuracy better than 0.01 m s^{-1}.

Time since deployment determines the depth of an XCP datum. We estimate the error in depth by matching temperature and velocity features in simultaneous XCPs. D'Asaro and Morehead (1991) found depth differences of about 2 m for a pair of XCPs dropped through adjacent holes in the Arctic pack ice. Since the NOAA WP-3D had only a single drop chute, AXCP pairs deployed during Ocean Storms exited a few seconds (a few hundred meters) apart. Two pairs were dropped; each showed depth differences of less than 2 m in the upper 200 m and less than 4 m in the 600–1000 m depth range.

Above about 50 m, surface wave velocities often dominate the signals measured by XCPs. Although this signal can be partially removed by fitting a surface wave profile to the data (Sanford et al. 1987), this technique is ineffective here, as the mixed layer is too shallow. We choose instead to ignore AXCP data above 50 m.

Frequency spectra. We will need frequency spectra of velocity to interpret the AXCP profiles. Spectra of horizontal velocity from the OSU mooring for days 278–304 (Fig. 3) reveal a strong inertial peak at all depths, a slight shoulder corresponding to the semidiurnal tide, a broad peak near $2f$, and the usual internal wave band. The near-inertial frequencies are clearly the most energetic component. Figure 4 shows the energy in the subinertial (<1.33 cpd), inertial (1.33–1.66 cpd), and superinertial (>1.66 cpd) frequency bands

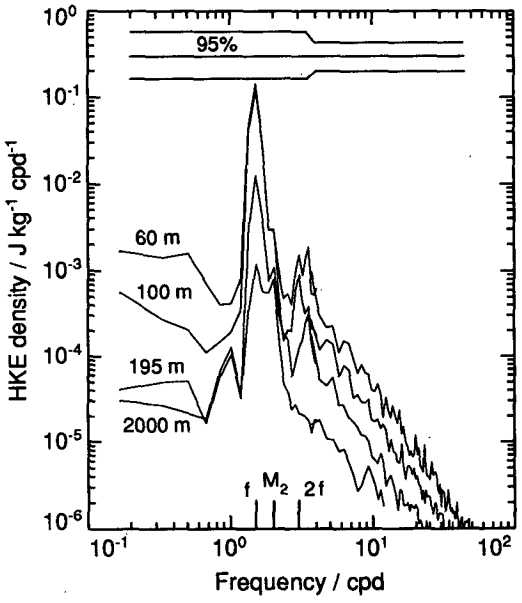

FIG. 3. Horizontal kinetic energy spectra from current meters on OSU mooring at 60 m, 100 m, 195 m, and 2000 m for days 278–304. The spectra are computed from 6-day long, half-overlapped pieces windowed with a half-cosine.

as a function of depth for data on days 277–304 from the OSU mooring. The mixed layer subinertial and inertial kinetic energy is estimated from the drifter data and the mixed layer superinertial energy from the 60-m VMCM data. The inertial band contains more than 80% of the energy at all depths in the upper 150 m, but drops to about 50% of the energy below 1000 m.

We interpret the referenced AXCP velocities as inertial currents plus an error due to noninertial components and AXCP errors. We reference the relative AXCP velocity profiles to the 1400–1600-m average velocity, thus making them absolute with a depth-independent error equal to the rms currents at this depth, about 0.045 m s^{-1} (Fig. 4). Alternative schemes—such as using the velocities directly from the AXCP, equivalent to using the electromagnetically determined barotropic flow as a reference, or using different reference levels—make little difference in the results.

The high-frequency internal waves have horizontal coherence scales that are short compared with the AXCP spacing (D'Asaro and Perkins 1984) and therefore contribute a random error of about 0.07 m s^{-1} at 100 m.

We partially remove the low-frequency contribution to each AXCP profile by interpolating the near-surface velocity field from the drifters (Fig. 1) to the position

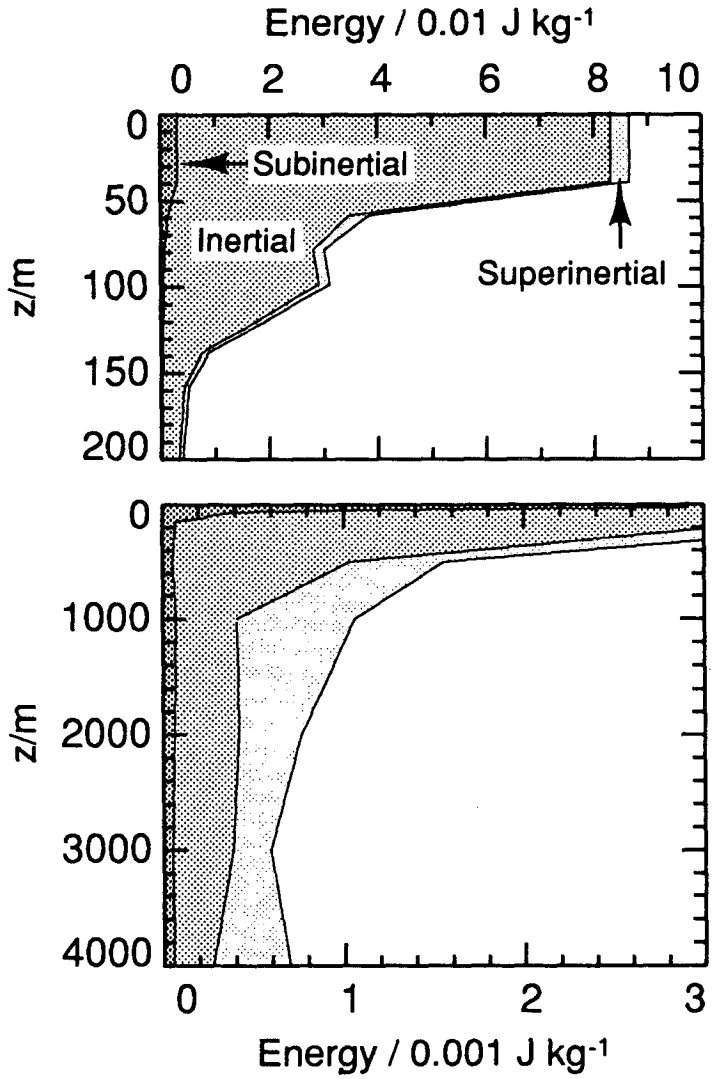

FIG. 4. Partition of horizontal kinetic energy by subinertial, inertial, and superinertial frequency bands in the upper (top panel) and deep ocean (bottom panel). Below 60 m, spectra from current meters on the OSU mooring for days 277–304 are used. The inertial band is 1.33–1.66 cpd. In the mixed layer, data from surface drifters are used. The mixed layer superinertial energy is taken from the 60-m deep current meter on the OSU mooring.

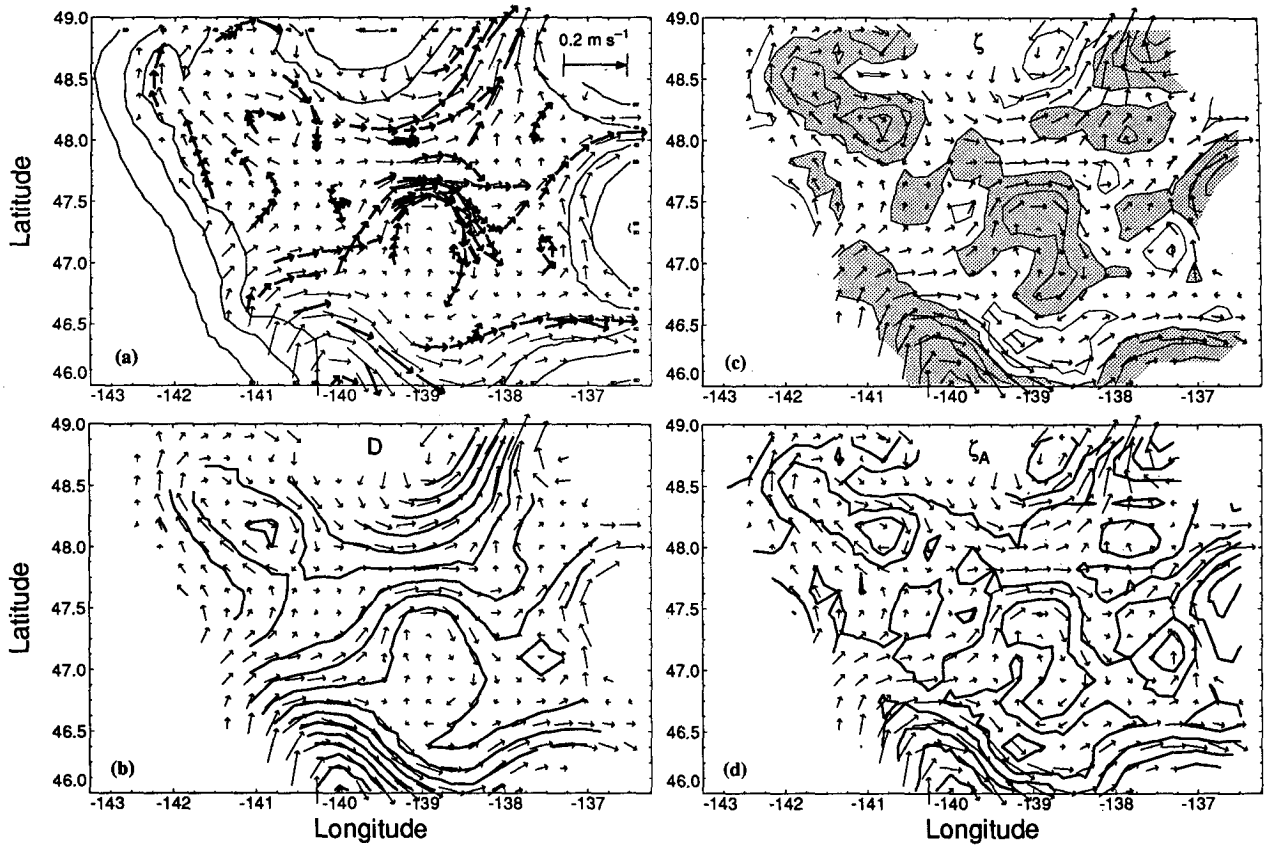

FIG. 5. Analysis of subinertial velocities from mixed layer drifters for days 280–300. (a) Subinertial velocity smoothed and sampled every 4 days (heavy arrows). An objectively analyzed field of vectors (light arrows) is computed from these. Only data with less than 60% error are shown. Contours of 80%, 60%, and 40% error are plotted. (b) Surface dynamic height contours derived from velocity data and mapped velocity arrows from (a); contour interval is 1 dynamic centimeter. (c) Relative vorticity and mapped velocity arrows from (a); contour interval is 1% of f, and negative values are shaded. (d) Absolute vorticity and mapped velocity arrows from (a); contour interval is 2% of f.

of each AXCP. The geostrophically determined subsurface velocities are highly correlated with the surface flow (section 4b), so we construct a profile of velocity at each AXCP based on this correlation and subtract it from each AXCP profile. We backrotate the residual to 0000 UTC day 278 at the inertial frequency corresponding to 47.5°N. The residual low-frequency error is less than the rms variability of the low-frequency velocity, 0.06 m s^{-1}.

We bound the error in AXCP inertial velocity from above as that due to all of the preceding factors, or 0.1 m s^{-1}; the error is probably less than this since we have partially compensated for the low-frequency flow and because the error in referencing is correlated with the other errors. We bound it from below as larger than the high-frequency error alone, 0.07 m s^{-1}. We check these bounds by applying the same procedure to the instantaneous moored velocity profiles from the PCM and OSU moorings at the time of the AXCP survey. In the 60–200 m depth range, the resulting profiles differ from the true demodulated inertial vector profiles by 0.04 and 0.07 m s^{-1} rms, for the OSU and PCM moorings, respectively, with maximum errors of 0.09 and 0.14 m s^{-1}.

4. Subinertial velocity

a. Measured

The heavy arrows in Fig. 5a show all subinertial velocities from the drifters and mixed layer velocities from moorings C, N, and W from days 280 to 300. For each record the data have been low-pass filtered using a cubic smoothing spline with a 4-day smoothing parameter and subsampled every 4 days. The resulting 212 vectors form a consistent flow field, with nearby vectors almost always having similar magnitudes and directions. We thus trade temporal for spatial resolution and treat all the data together. These vectors are objectively mapped following Bretherton et al. (1976), assuming that the true velocity field is nondivergent and is characterized by the analytical correlation functions from McWilliams (1976a,b) and Shen and McWilliams (1978). Transverse and longitudinal corre-

lation lengths of 150 and 40 km, respectively, and an instrumental error of 5% were used (see the appendix). This analysis produces fields of horizontal velocity (Figs. 5a–d), streamfunction normalized to equal dynamic height at 47.5°N (Fig. 5b), relative vorticity (Fig. 5c), and absolute vorticity $\zeta_A = \zeta + f$ (Fig. 5d). We plot only data for which the mapping error is less than 60%. Most of the domain has a mapping error between 20% and 40%.

Figure 5 shows a subinertial flow that is northward and eastward with embedded eddies. The spatial mean flow is 0.027 m s^{-1} to the northeast, and the rms eddy velocity about this mean is 0.053 m s^{-1}. The vorticity field shows the eddies to be dominantly anticyclonic with an rms vorticity of $0.023f$ and a maximum anticyclonic vorticity of $-0.07f$ at the bottom left of the domain. The strain field (not shown) has smaller correlation spatial scale, about 20 km, but an rms value comparable to vorticity. A large-scale straining $\overline{v}_y \approx 0.005f$ is apparent in the acceleration of buoys out of the domain to the north and to the south.

The eddies have a typical scale of about $L = 40$ km and thus a Rossby number, $\mathrm{Ro} = U/fL$, of about 0.01. We expect the flow to be geostrophic and nearly nondivergent as assumed. The vorticity equation appropriate for low Rossby number flow,

$$\frac{D(\zeta + f)}{Dt} = -(\zeta + f)\nabla \cdot \mathbf{u}, \qquad (12)$$

implies that $\nabla \cdot \mathbf{u}$ is a factor of Ro smaller than the vorticity. We used this as a consistency check on the assumptions of the objective analysis. The streamline and absolute vorticity fields (Figs. 5b and 5d) are well correlated. The residual in absolute vorticity from this correlation is $0.015f$, only slightly above the estimated mapping error of $0.013f$. Therefore, ζ_A is constant along streamlines to within the measurement error. This supports our assumption that the subinertial, near-surface flow is steady and nondivergent over 25 days.

b. Geostrophic velocity

CTD data taken on days 273–280 provide a second estimate of the subinertial surface flow. Figure 6 shows contours of surface dynamic height relative to 800 dbars objectively mapped (Bretherton et al. 1976) using a Gaussian correlation function with a 100-km scale (see the appendix). The pattern is similar to, but somewhat smoother than, the dynamic height computed from the velocity data in Fig. 5b. The anticyclonic eddy near the moored array (47.5°N, 139°W) is not evident in the CTD data, probably because it fits between the CTD stations and is thus poorly sampled. The CTD-derived and buoy-derived surface dynamic heights are correlated with $r = 0.9$, a slope of 1.06, and a residual error of 1.2 dyn. cm. For deeper reference levels to 1500 dbars the correlation is equally good but the CTD-derived dynamic height is too large; for shallower levels to 500 dbars it is too small. The flow in the upper 1500 m is therefore taken to be nearly geostrophic with a level of no motion near 8 MPa. Matear (1993) obtains similar results using a full inverse of these data.

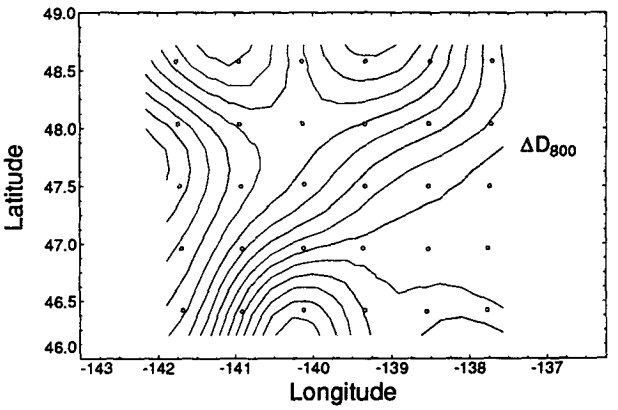

FIG. 6. Dynamic height relative to 800 dbars from CTD data taken on days 273–280. Station positions are indicated by the circles. Contour interval is 1 dynamic centimeter.

The estimated geostrophic velocities do not resolve velocity features with the scale of the Rossby radius (40 km), since the CTD station spacing was 60 km. Thus, although the surface geostrophic velocity field is correlated with the drifter-derived velocity field, the surface geostrophic kinetic energy is only 34% of that measured directly. Most of the kinetic energy is therefore contained in features with about the Rossby radius scale. Subinertial velocities measured on the moorings are not strongly correlated in the vertical, unlike the geostrophic velocities. This suggests that only the subinertial velocities with scales larger than the Rossby deformation radius are vertically coherent, while the smaller-scale motions have a more complex structure.

5. The storm

Figure 7 shows the wind stress and the inertially backrotated currents predicted from it using (1) with $r = 0$. We choose $H = 55$ m based on the observed vertical profile of horizontal current measured after the storm (section 7). We define the backrotated inertial current vector as

$$\tilde{U} = \tilde{u} + i\tilde{v} = (u + iv)e^{if_0(t-t_0)}, \qquad (13)$$

with f_0 equal to the inertial frequency at 47.5°N and t_0 defined as the start of day 278. If u and v were a pure inertial oscillation at this latitude, then $\tilde{u}$ and $\tilde{v}$ would be constant. The inertial speed is $|\tilde{U}|$ and the phase of $\tilde{U}$ corresponds to the direction of the inertial currents at t_0.

The storm on day 277 is the only large wind event in the region during October 1987. The predicted mixed layer inertial currents after the storm are about 0.6 m s^{-1}. The winds are weak for the next 25 days,

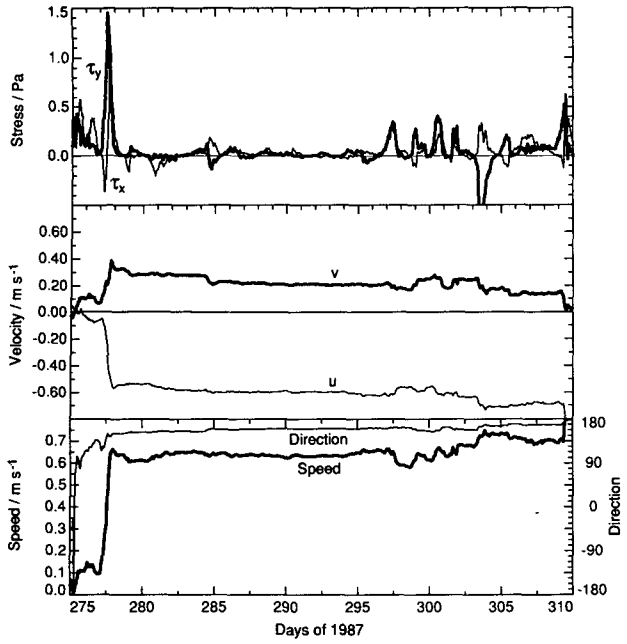

FIG. 7. Wind stress and inertial current generation. (a) Wind stress (Large et al. 1995) at mooring C. (b) Inertially backrotated east and north velocity components predicted from (1) with $r = 0$ and $H = 55$ m. (c) Corresponding speed and direction.

with (1) predicting a change of about 0.1 m s^{-1} in the inertial current due to the wind, mostly in the sense to rotate $\tilde{U}$ counterclockwise. We can ignore the wind forcing through about day 297. The wind forcing increases thereafter, with larger storms occurring on days 303 and 309.

A surface isobar chart at day 277.5 (Fig. 8) shows the structure of the storm. This was constructed using all available surface wind and pressure measurements and satellite photographs (N. Bond 1990, personal communication). A cold front rotating around a low to the north of our area moves eastward over the site preceded by a warm front. The main wind shift occurs at the cold front; this is preceded by a smaller wind shift at the warm front. The relative timing of these shifts makes this storm a particularly effective generator of mixed layer inertial currents (Crawford and Large 1995). From analyses based on satellite imagery and surface reports, the junction of the warm and cold fronts translates at 18.5 m s^{-1} toward 63°T. The cold front itself translates almost due eastward at about 16 m s^{-1}. It is difficult to estimate the errors in these numbers, but 2–3 m s^{-1} and 15°–20° are reasonable.

6. Stratification

a. Temperature and density

The evolution of the density and temperature in the upper 200 m at the PCM and OSU moorings is shown in Figs. 9c, 9d, and 10d. The isotherms and isopycnals spread and deepen in the upper 80 m during the storm on day 277 and for several days thereafter. A more detailed analysis of the associated mixing is given by Crawford and Large (1995) and Large and Crawford (1995). Before and after the storm, the isopycnals are remarkably free of subinertial variations, consistent with the low levels of mesoscale activity. Some activity is evident in the PCM data near day 275 and in the OSU data near day 300. This activity may be related to the near-surface fronts that appear both in the drifter data (Paduan and Niiler 1993) and in closely spaced profiles of density (W. Crawford 1993, personal communication).

b. Mixed layer depth

CTD profiles taken on days 277–280 (Tabata et al. 1988; Matear 1993) measured mixed layer depths after the storm. Five profiles were taken within 30 km of the OSU mooring; they showed mixed layer depths ranging from 33 m to 43 m. Fifteen profiles were taken within 120 km of the moorings; they showed mixed layer depths from 33 m to 49 m. The AXCP survey on day

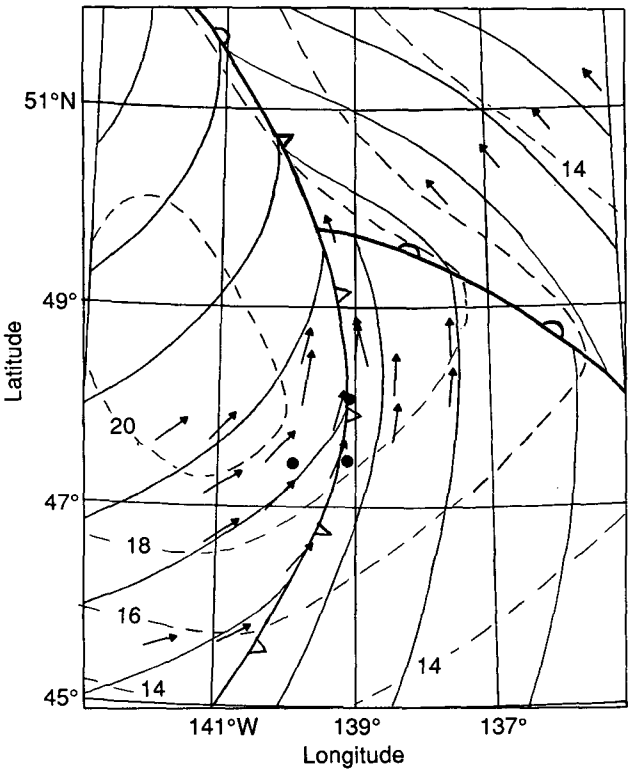

FIG. 8. Surface chart for 1200 UTC, day 277. All wind and pressure observations from 1000 UTC to 1400 UTC are used. Observations are advected by the mean speed of the storm to their estimated position at 1200 UTC. Heavy lines give frontal positions; dashed lines give wind speed contours; arrows are wind speed measurements. Large dots are mooring positions.

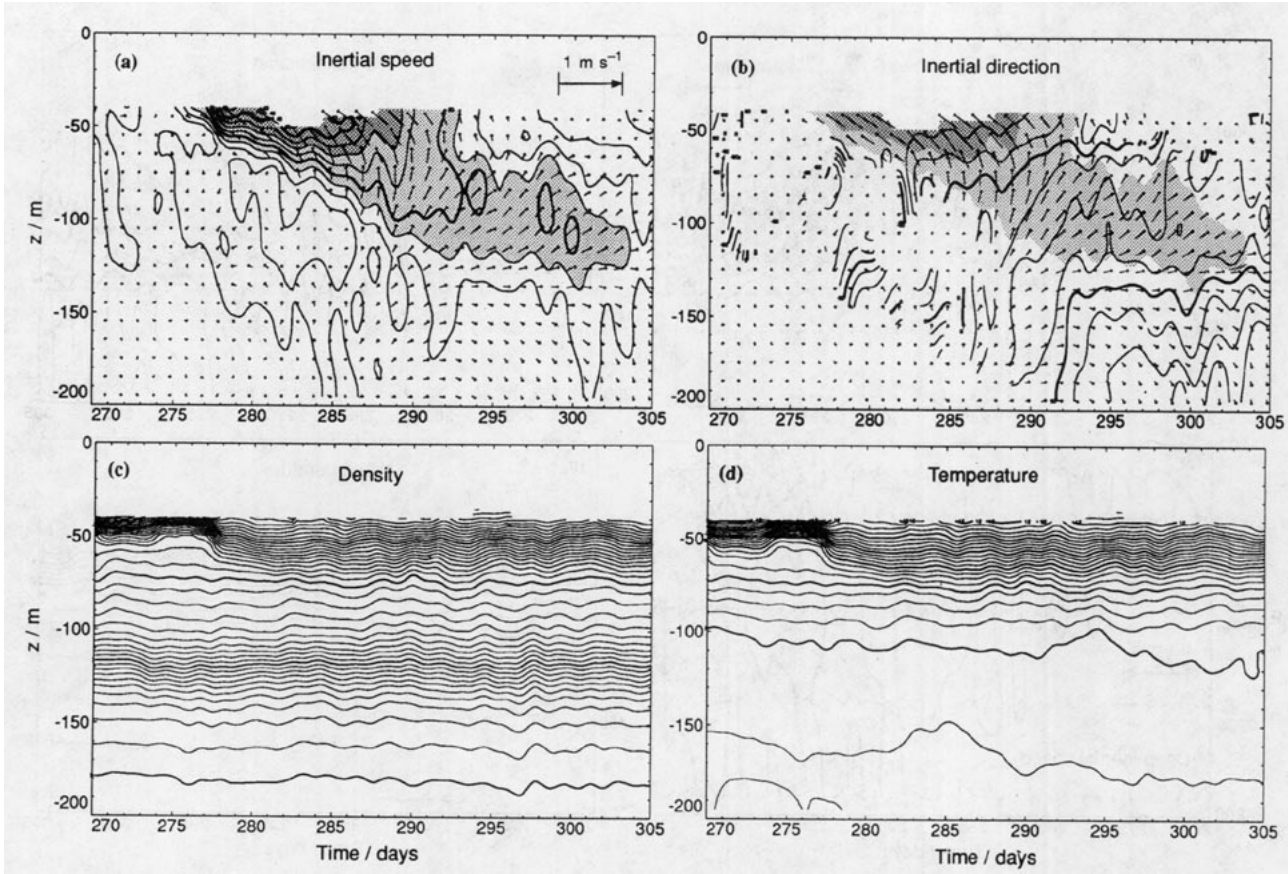

FIG. 9. Data from PCM mooring. (a) Backrotated inertial vectors with contours of inertial speed. Speeds greater than 0.15 m s^{-1} are shaded; contour interval: 0.05 m s^{-1}. (b) Backrotated inertial vectors, shading from (a), with contours of backrotated inertial direction; contour interval: 22.5°. (c) Density contours; interval: 0.05 kg m^{-3}. (d) Temperature contours; interval: 0.25°. Day 277 is 4 October.

298 measured mixed layer depths ranging from 35 m to 40 m; in some profiles the mixed layer is poorly defined. This variability is comparable to the 8 m, peak to peak, tidal and inertial frequency displacements in the upper thermocline measured in the PCM data. Moored temperature data at mooring C show an average mixed layer depth of about 35 m during this period. The average mixed layer depth is thus a few meters above the top of the PCM mooring (40 m).

7. Inertial currents

a. Moored

The backrotated inertial vectors from the moorings (Figs. 9 and 10) show the evolution of the inertial currents in response to the storm. The pattern of inertial current evolution is similar at all moorings, including the ADCP mooring (R. Davis 1993, personal communication). In each, inertial currents are generated in the mixed layer by the storm and spread downward into the thermocline over the next 30 days. We describe the evolution of the inertial currents in a series of stages:

Generation. The storm on day 277 generates inertial currents in the upper ocean. These currents penetrate to about 60 m, well below the mixed layer, at both moorings (Figs. 9a, 10a). The thermocline warms during the storm to the same depth (Figs. 9d, 10d). Crawford and Large (1995) and Large and Crawford (1995) attribute these changes to turbulent mixing that penetrates below the mixed layer.

Spreading. For the first week after the storm (days 278–285), the inertial currents spread slowly downward into the thermocline with only a slight clockwise veering of the backrotated inertial vectors with depth, that is, a slightly negative phase shift in $\tilde{U}$. The inertial currents penetrate to about 75 m by day 284. The density and temperature profiles change only slightly during this time.

Formation of the beam. On about day 284, the isolines of mixed layer inertial current speed begin to spread as the inertial currents move more rapidly into the upper thermocline. This is more apparent at the OSU than at the PCM mooring. By day 300 the strongest inertial currents are at 100 m and little energy remains in the mixed layer. During this period, the frequency of the inertial currents rises from about f to

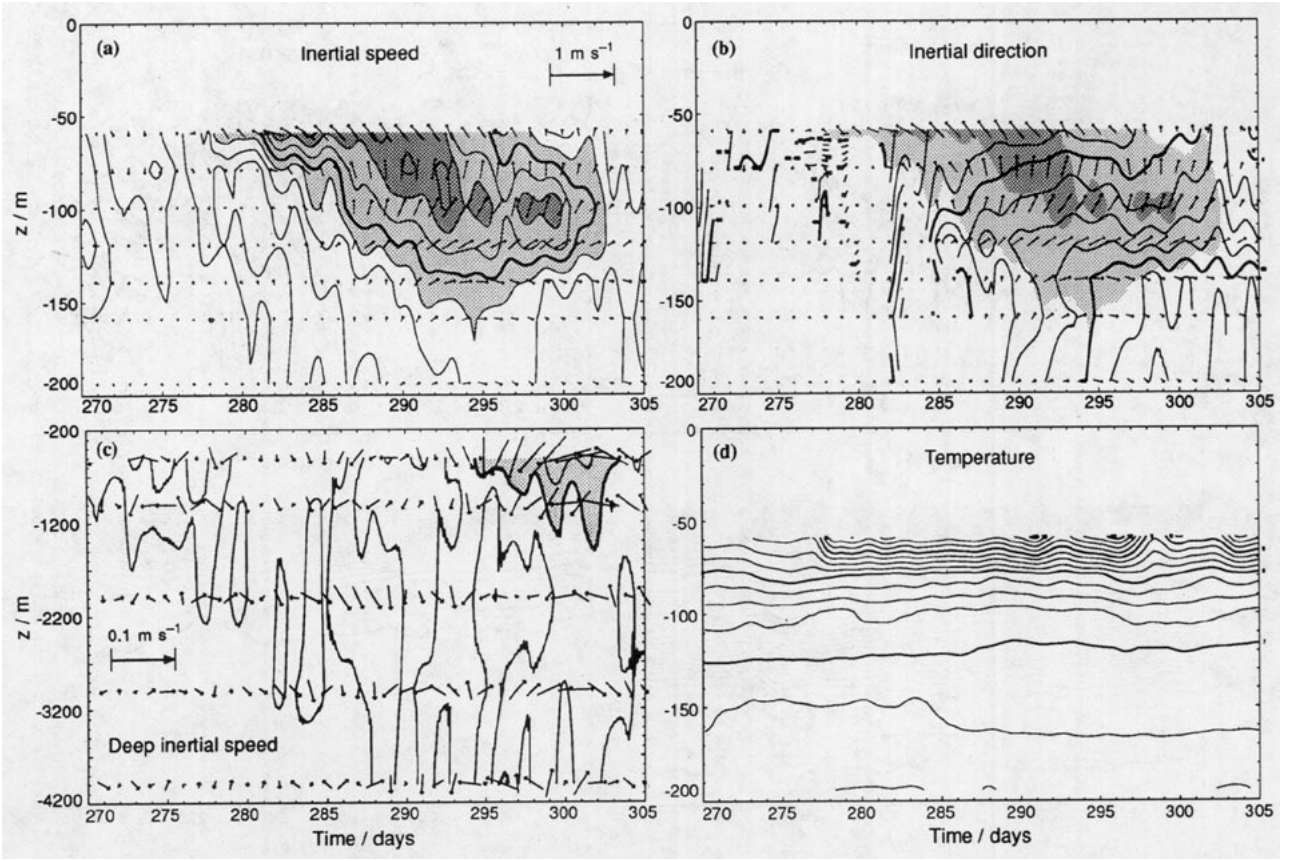

FIG. 10. OSU moored data. (a) Backrotated inertial vectors with contours of inertial speed, 0–200 m. Speeds greater than 0.15 m s^{-1} are shaded; contour interval: 0.05 m s^{-1}. (b) Backrotated inertial vectors, shading from (a), with contours of backrotated inertial direction; contour interval: 22.5°. Contours are not shown for speeds less than 0.1 m s^{-1}. (c) Backrotated inertial vectors with speed contours 200–4200 m. Speeds greater than 0.05 m s^{-1} are shaded; contour interval: 0.025 m s^{-1}. (d) Temperature contours; interval: 0.25°.

roughly $1.01f$, as can be seen from the rate of turning of the backrotated inertial vectors. The 100-m inertial currents lead those in the mixed layer by roughly 60°. This pattern resembles a beam, or packet, of near-inertial waves propagating downward from the mixed layer. We name this thermocline maximum in near-inertial energy "the Beam."

Persistence of the Beam. From day 295 to 305, the Beam persists with some weakening and a slight deepening. The wind forcing increases after day 298. Stronger storms pass over the Ocean Storms area after day 305, new inertial motions are generated, and the evolution of the inertial motions due to the storm can no longer be followed.

1) DEEP INERTIAL CURRENTS

The deep data from the OSU mooring (Fig. 10c) suggest a weak increase in inertial energy that extends to the ocean bottom [see also Levine and Zervakis (1995)]. A downward extension of the Beam, with enhanced inertial currents and clockwise veering with depth, extends to about 1000 m. Below this, there is little correlation between the deep inertial currents and the strong, storm-driven upper ocean.

2) INERTIAL SHEAR

The inertial shear, computed from the vertical first difference of the backrotated inertial vectors in Fig. 9, is shown in Fig. 11. The storm generates a strong inertial shear between the mixed layer base and about 70 m. The shear deepens and weakens through day 285 and weakens further thereafter. By day 300 it is about one-fourth of its value on day 280, similar to its value before the storm. After day 300 the shear near 60 m increases again, probably because of renewed wind forcing.

b. Mixed layer

The drifter array measures the horizontal structure of the storm-forced inertial currents. Energetic inertial oscillations are obvious in the drifter tracks (Fig. 1). We use drifter 7944 at approximately 48.5°N, 140.4°W as an example. This trajectory is marked with a circled

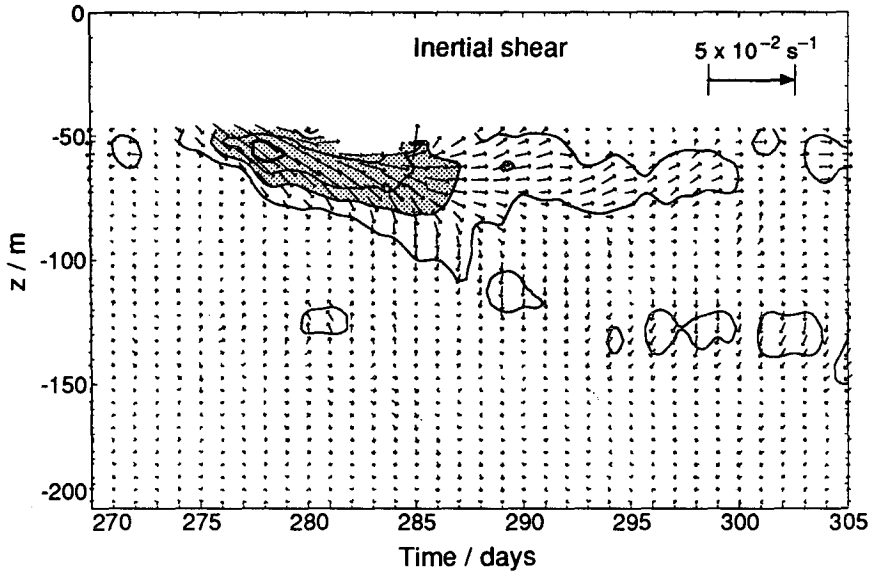

FIG. 11. Backrotated inertial shear vectors computed from vectors in Fig. 10. Shear vectors and contours of shear magnitude are plotted. Shear magnitudes greater than 2×10^{-2} s^{-1} are shaded. Contour interval: 5×10^{-3} s^{-1}.

"+" in Fig. 1. Before the storm (northwest end of track), the buoy drifts southeastward at 4–6 cm s^{-1} with superimposed inertial oscillations of comparable magnitude. Four inertial periods from the start of the track, the inertial oscillations increase dramatically as the storm passes over the buoy. The inertial circle is about 14 km in diameter, implying an inertial velocity of about 0.7 m s^{-1}. The currents remain this large for about 10 days, and then slowly decrease, reaching prestorm levels about 20 days after the storm. A similar pattern occurs at each of the drifters, although those deployed after the storm do not show the prestorm conditions.

For each drifter and mooring, we compute the backrotated inertial current vector (13) as described in section 3. The panels of Fig. 12 show these vectors for days 276–300 at 5-day intervals. The speed and direction contours show the results of objectively mapping these vectors using a Gaussian correlation function with a 90-km scale and 10% measurement error. The correlation scales of the data change dramatically with time, but we have not accounted for this in our mapping.

Before the storm (Fig. 12a) the mixed layer backrotated inertial vectors have a nearly uniform amplitude (0.1 m s^{-1}) and direction. Two days after the storm (Fig. 12b) they are much more energetic (0.35–0.7 m s^{-1}) and still nearly uniform across the array. Clearly the storm has accelerated inertial currents within the mixed layer with approximately the magnitude predicted in Fig. 7. These have a horizontal scale of hundreds of kilometers, comparable to the scale of the storm (Fig. 8), and smaller-scale variations.

Between days 280 and 285 (Figs. 12b and 12c), the amplitude of the backrotated mixed layer inertial vectors does not change significantly, but their direction develops a pattern of clockwise rotation toward the north. This pattern intensifies through day 295 (Figs. 12d and 12e) as the amplitude decays. The rate of decay is slowest in the northwest quadrant of the array and fastest in the southeast. By day 300 (Fig. 12f), the mixed layer inertial currents have decayed to nearly their prestorm level.

c. *Mixed layer energy and wavenumber*

The backrotated inertial vectors in Fig. 12 have a nearly constant amplitude and a direction that varies linearly in space. This suggests their spatial structure can be accurately described by a plane wave.

We fit a single plane wave

$$\tilde{U}(x, y) = \tilde{U}_{\text{fit}} e^{i(kx+ly)} + U_R(x, y) \qquad (14)$$

to these data using the algorithm described in the appendix. Here $\tilde{U}_{\text{fit}}$ is the complex wave amplitude, k and l are the wavenumbers, and U_R is a residual. The phase of $\tilde{U}_{\text{fit}}$ is set by referencing x and y to a point near the center of the array (47.5°N, 139.5°W).

Figure 13 shows the parameters of (14) for days 276–300. The number of data points increases from 14 on day 276 to about 40 on day 285. The energy in the fit $E_{\text{fit}} = \frac{1}{2}|U_{\text{fit}}|^2$ (shading) is more than 90% of the total energy E_{tot} through day 290. (There is some imprecision here since E_{tot} is the average of the energies of the irregularly spaced buoys.) After day 295, the fit energy is less than half of the total, so (14) does not

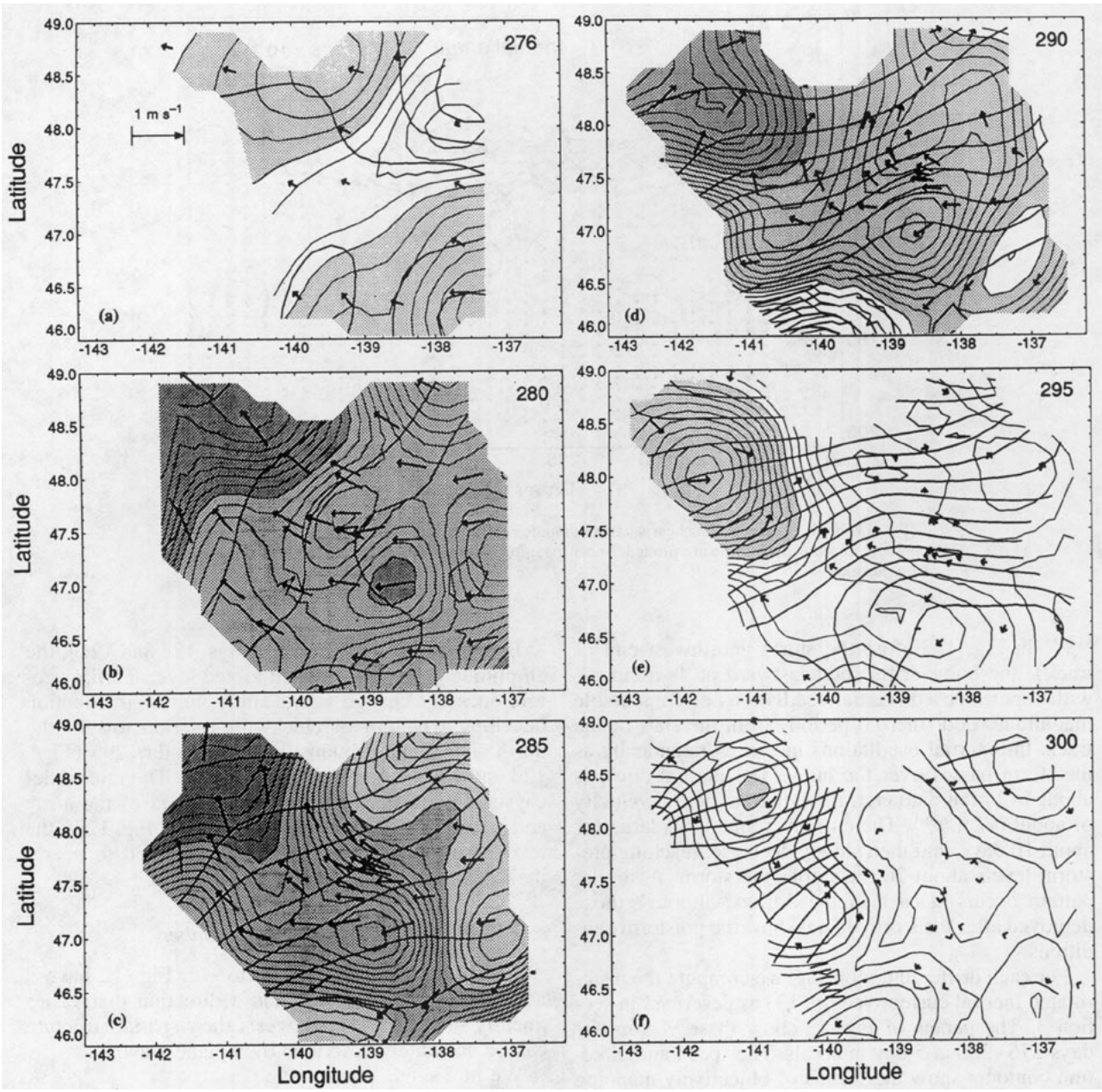

FIG. 12. Evolution of mixed layer inertial currents. Each panel shows mixed layer inertial current from drifters and moorings (arrows) and speed and direction contours from an objective mapping of these data. Time in days of 1987 is indicated in upper right-hand corner. Only regions with an error less than 80% are shown. Speed contour interval is 0.02 m s^{-1}. Direction contour interval is 22.5°. Speed contours are shaded starting at 0.02 m s^{-1} and darkened starting at 0.04 m s^{-1}.

describe the field well. The uncertainties in the parameter values are indicated by the symbols, which show the results of fitting 40 realizations of a Monte Carlo simulation of the data as described in the appendix. The 2nd and 39th ranked realizations are approximate 95% confidence limits. By about day 297, these become sufficiently large to make the fits nearly meaningless.

Both total energy and the energy in the fit increase dramatically on day 277 because of the storm. For the next 23 days the energy decreases, slowly at first, then more rapidly; by day 300, $|\tilde{U}_{\text{fit}}|$ is about 0.05 m s^{-1}. The period of most rapid decrease, days 285–290, corresponds to the time of formation of the Beam as seen in Figs. 9 and 10. The direction, that is, the phase, of $\tilde{U}_{\text{fit}}$ increases slightly at first, corresponding to a slightly subinertial frequency, and then decreases, corresponding to a frequency of about 1% above f, as the Beam forms. The horizontal wavenumbers are initially small,

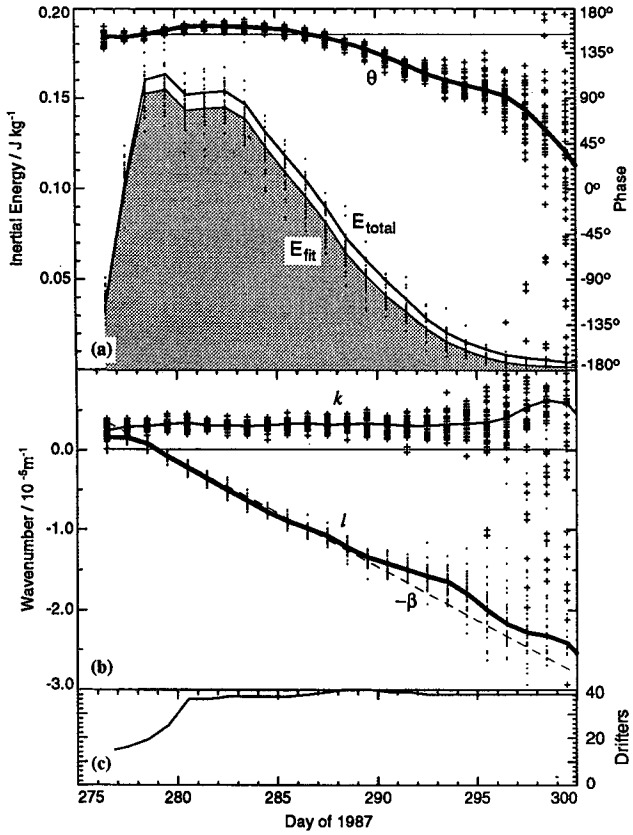

FIG. 13. Parameters of plane-wave fit to mixed layer inertial currents for all data. (a) Fit energy E_{fit} (shaded), total energy E_{tot} (line), and phase of U_{fit} (heavy line). (b) Wavenumbers k (light solid line) and l (heavy solid line). Diagonal dashed line labeled "$-\beta$" has a slope of $-\beta$. (c) Number of data points in fit. Symbols show parameters for 40 Monte Carlo simulations of the fit residuals and serve as confidence limits.

corresponding to a wavelength of about 1700 km. The north–south wavenumber l decreases steadily, while the east–west wavenumber k remains constant to within the confidence limits.

The decay rate of the mixed layer inertial currents is faster in some places than in others (Fig. 12). We therefore define four geographical subregions (NE, NW, STH, CL) in Fig. 1, each containing a subgroup of drifters and moorings. These regions were chosen to have approximately the same number of drifters while being geographically separated and having enough spread so that a spatial scale could be estimated for each subgroup of drifters. For each region, we fit (14) and display the fit parameters in Figs. 14–17. Statistically significant variations between these regions are apparent. The inertial currents are most energetic in NW and least in STH. They decay faster in CL and NE than in NW. Similarly, l is less negative in NW and more negative in CL.

d. Upper-ocean inertial currents on day 298

On day 298 a 125 km by 150 km region surrounding the moored array was surveyed using AXCPs (Fig. 2). We now describe the three-dimensional structure of the inertial velocity at that time.

1) MAPS

Figure 18 shows the backrotated inertial vectors from both AXCP and moored data. They form a consistent picture. At 100 m (heavy arrows) their amplitude is nearly constant at about 0.25 m s^{-1}, while their direction (contours) rotates counterclockwise to the SSE. This implies a horizontal wavenumber pointing in this direction. A similar pattern applies at 75 m (light arrow, smallest arrowhead) and 140 m (light arrow, largest arrowhead). Generally the direction rotates clockwise with increasing depth (i.e., with larger arrowheads), consistent with an upward pointing wavenumber.

2) SECTIONS

Sections of backrotated inertial vectors along each of the three legs of the AXCP survey (Fig. 2) are shown in Figs. 19–21. The sections are computed from

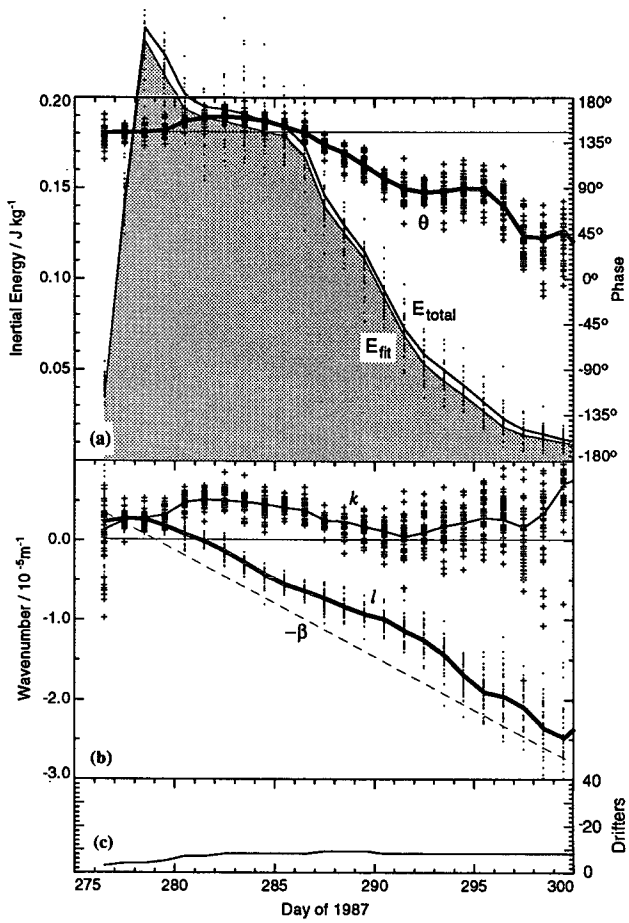

FIG. 14. Parameters of plane-wave fit to mixed layer inertial currents for subgroup NW.

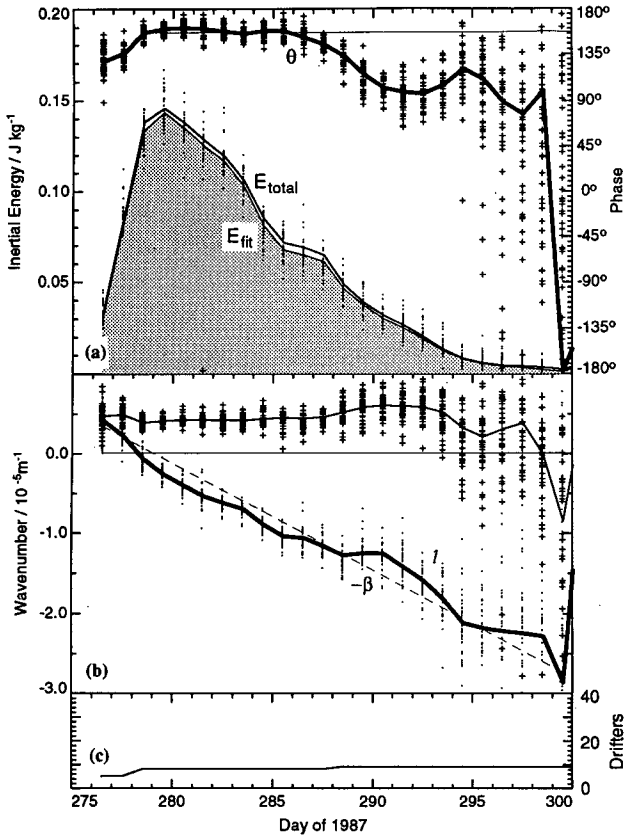

FIG. 15. Parameters of plane-wave fit to mixed layer inertial currents for subgroup NE.

moored, AXCP, and drifter backrotated inertial vectors; each drifter vector is reproduced at 15 m, 20 m, and 25 m. These data were horizontally interpolated to the section using two-dimensional smoothing splines (Craven and Wahba 1979) with essentially no smoothing. The location of the data along the section is indicated by triangles whose size indicates the perpendicular distance (0–20 km) from the section to the data.

The Beam is present everywhere in these data; every velocity profile has a maximum in inertial energy between 100 m and 150 m. Section A (Fig. 19) is oriented approximately perpendicular to the contours of the direction of the backrotated inertial vectors in Fig. 18, so it clearly shows the clockwise rotation of the direction to the north. The other two sections are nearly parallel to the contours of backrotated inertial direction and therefore show the progression less clearly. In all three sections, the clockwise rotation of the backrotated inertial vector with increasing depth is apparent.

For the most part, the inertial currents in the mixed layer are weak. In the few regions where they are strong enough that their direction is well determined (about 0.05 m s^{-1}), the backrotated mixed layer inertial vectors are about 90° clockwise of those in the Beam. Below the Beam, the inertial currents are also weak and have large errors.

3) WAVENUMBERS

We fit the backrotated vectors with a plane wave (14) at each depth as was done with the drifter velocities. The phase of $\tilde{U}_{\text{fit}}$ is set by referencing x and y to the position of the PCM mooring. The results are shown in Fig. 22. Confidence limits in these parameters were determined using a Monte Carlo simulation as described in the appendix. The small symbols give the parameter values from 50 such realizations; 95% confidence limits are located between the second and third and 47th and 48th ranked values. The difference between the energy in the fit (shaded region, top panel) and the total energy (line, top panel) is about 0.007 J kg^{-1} near 100 m, which is about three times the estimated demodulation error of 0.0025 J kg^{-1} (0.07 m s^{-1}). Equivalently, the fit explains about 75% of the inertial energy, when corrected for the noise energy.

The maximum in inertial energy near 110 m is the Beam. The directions of the backrotated inertial vectors are about 130° clockwise of the vectors initially generated by the storm, and turn approximately 135° clock-

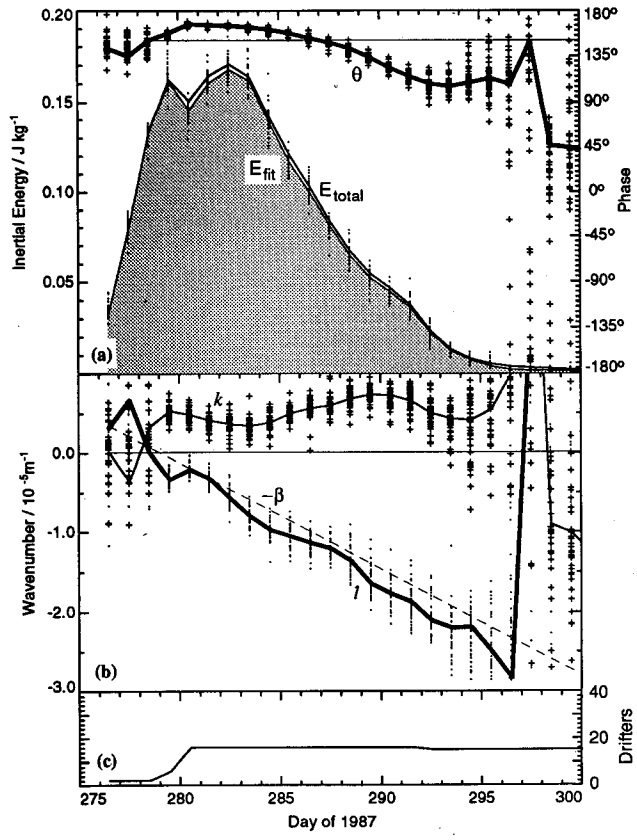

FIG. 16. Parameters of plane-wave fit to mixed layer inertial currents for subgroup CL.

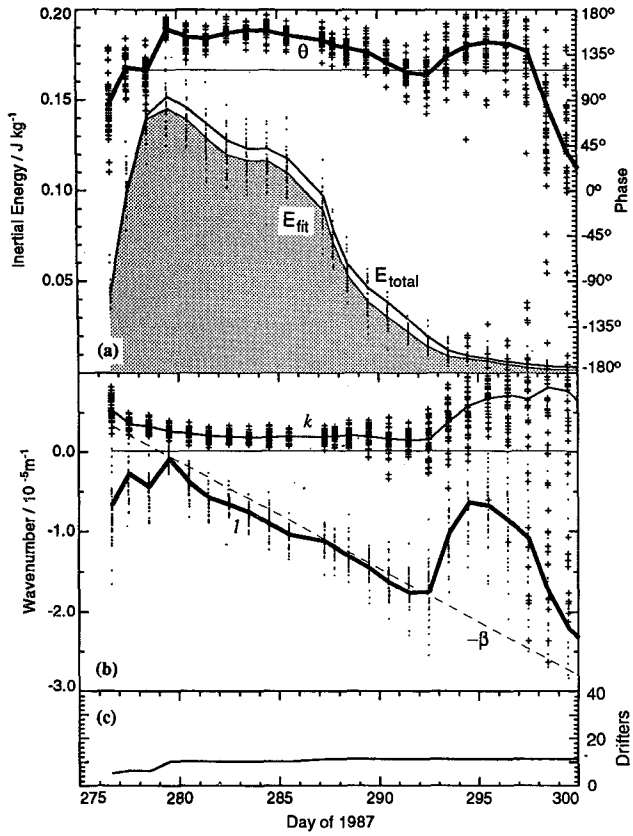

FIG. 17. Parameters of plane-wave fit to mixed layer inertial currents for subgroup STH.

wise between 80 m and 140 m. The peak speed is about 0.22 m s^{-1}, and the half-energy width is about 80 m. Above the Beam, the inertial direction rotates clockwise upward about 70° into the mixed layer, although this number is less reliable than it appears, owing to the very weak mixed layer inertial currents at this time. Below 140 m, the backrotated inertial direction rotates clockwise, and the wavenumber points roughly SE but the estimates are barely significant. The velocity difference between 40 m and 70 m is 0.007 s^{-1}, comparable to that observed at the same time at the PCM mooring (Fig. 9).

The k and l wavenumbers are nearly constant in the depth interval of the Beam and are statistically indistinguishable from those in the mixed layer at this time (Fig. 13). The horizontal structure of the inertial currents in the upper 150 m appears to be accurately described by a single plane wave whose wavenumber varies with time.

4) SPATIAL VARIABILITY

The spatial structure of the inertial currents is not totally described by the plane-wave fit. The maximum speed in the Beam varies (0.1–0.3 m s^{-1}) as does its depth (95–140 m). These variations are spatially coherent, as seen by the speed contours in Fig. 18, unlike the error, which is dominated by incoherent internal wave noise. Furthermore, the maximum inertial speeds in the Beam on day 298 measured at the two moorings differ by 10 cm s^{-1}, greatly exceeding the measurement error.

8. Dynamical tests

a. *Storm forcing*

The storm on day 277 generates inertial currents in the mixed layer. The slab model (1) using the winds at mooring C predicts an amplitude of about 0.6 m s^{-1} (Fig. 7), comparable to the 0.50–0.58 m s^{-1} observed in the CL cluster (Fig. 16). If we model the wind as due to a storm of fixed shape that translates over the ocean with a velocity $\mathbf{G}$, then (1) implies that the resulting mixed layer inertial currents will have a phase speed, $c = f/\alpha$, equal to $|\mathbf{G}|$ and a horizontal wavenumber with the same direction as $\mathbf{G}$. Extrapolating the wavenumbers in Fig. 13 to the time of the storm, day 277.5, we estimate $c = 29 \pm 5$ m s^{-1} on a heading of 73 ± 10°T. This is about 50% faster than the meteorological estimate of the storm advection speed, 18.5 m s^{-1}, but in approximately the same direction. We conclude that the assumption of a fixed shape, translating storm is not very accurate here, unlike the results found by Kundu and Thomson (1985). The winds of this storm rotate at almost exactly the inertial frequency and are therefore very efficient generators of mixed layer inertial currents (Crawford and Large 1995). The amplitude and phase of these currents are therefore quite sensitive to the details of the wind field, perhaps explaining the observed difference between c and $|\mathbf{G}|$.

b. *The β effect*

The spatial structure of the mixed layer inertial currents is easily explained following D'Asaro (1989). The wind stress pattern associated with the storm has a spatial scale that is large compared with that of the array and moves across the array in a small fraction of an inertial period. Accordingly, the inertial currents generated by the storm have a scale that is large compared with the array's. If we assume that the inertial currents rotate at the local inertial frequency, but that f varies as $f_0 + \beta y$, then

$$\tilde{U} \approx e^{i\beta y(t-t_0)}. \tag{15}$$

The north–south wavenumber l decreases as $-\beta t$, while the east–west wavenumber k remains constant. A 180° phase change across a 300-km array will occur in 8 days, in rough agreement with the observations.

More quantitatively, the dashed lines in Figs. 13–17, with a slope of $-\beta$, explain almost all of the decrease in the north–south wavenumber l. The β effect therefore explains the dramatic shortening of the hori-

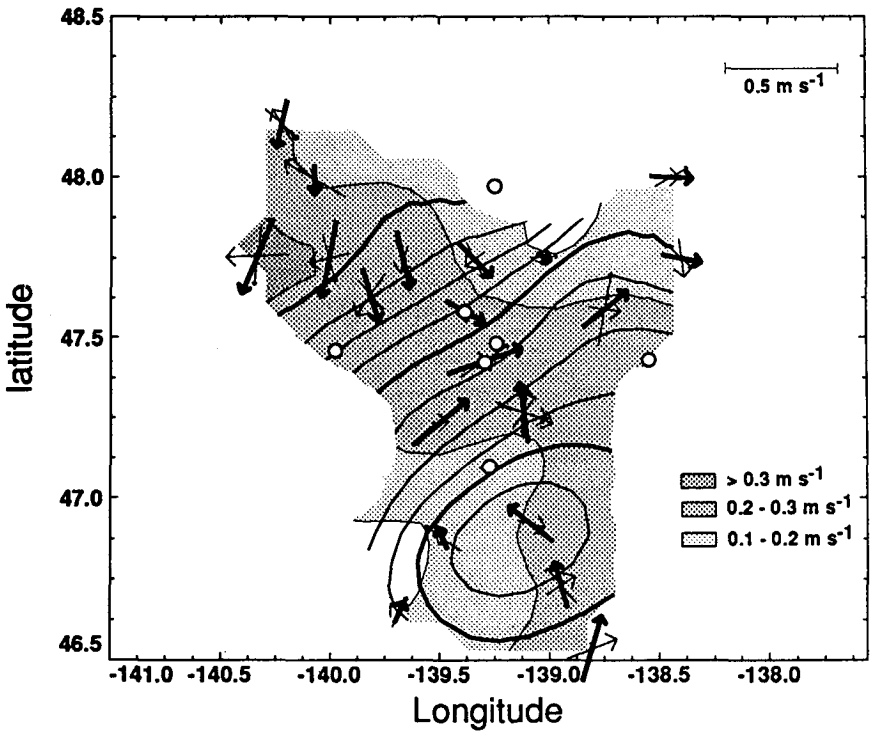

FIG. 18. Backrotated inertial vectors from AXCP and moored data on 25 October, day 298, at 80 m (light, small arrowhead), 100 m (heavy, medium arrowhead), and 40 m (light, large arrowhead). Direction at 100 m is contoured; contour interval is 22.5°. Speed at 100 m is shaded and contoured; contour interval is 0.1 m s^{-1} and the shading starts at 0.1 m s^{-1}. Mooring locations are indicated by white circles.

zontal scale of the mixed layer inertial currents following the storm.

c. *Modal analysis*

The primary goal of this paper is to test whether linear internal wave theory can explain the observed evolution of the near-inertial velocity field. The most direct way to do this would be to decompose the velocity field into vertical modes, as in (3), and ask whether the modal amplitudes obey (4). We have attempted such an analysis, but the results were unsatisfactory, as the computed modal amplitudes were quite noisy. We believe that this is because our data have insufficient vertical resolution. Figure 23 shows the vertical structure of the first four baroclinic modes. The locations of the OSU current meters are indicated by the heavy dots. In the deep ocean, the vertical spacing of the current meters is 1000 m. This array can resolve only the first few modes, since higher modes have wavelengths shorter than the array's Nyquist wavelength of 2000 m. High mode energy in the deep ocean will be aliased into the resolvable modes. In our analysis, for example, substituting white noise for the data at all the current meters produced a modal decomposition with most of the energy in the lowest four modes. The most interesting signal in the data is concentrated in the upper few hundred meters; the first four modes are clearly insufficient to resolve this structure.

A proper analysis of (4) requires that we know the horizontal structure of each mode. However, we have good measurements of the horizontal structure of the inertial currents only in the upper 200 m. There is no reason to suppose that the deep currents will have the same horizontal structure, particularly since they are poorly correlated with the upper ocean currents.

Although a modal analysis is the most obvious way to test the applicability of linear theory, our sampling array has insufficient vertical and horizontal resolution. We have chosen, therefore, to concentrate on comparing the observed spatial structure in the upper ocean with that predicted by linear theory.

d. *Gill's (1984) analysis*

Gill (1984) predicts the approximate residence time (9) of mixed layer inertial currents based on their horizontal scale. In our data, the horizontal scale of the inertial currents varies rapidly in time. Following D'Asaro (1989), we modify (8) so that the phase of the nth mode at time t is

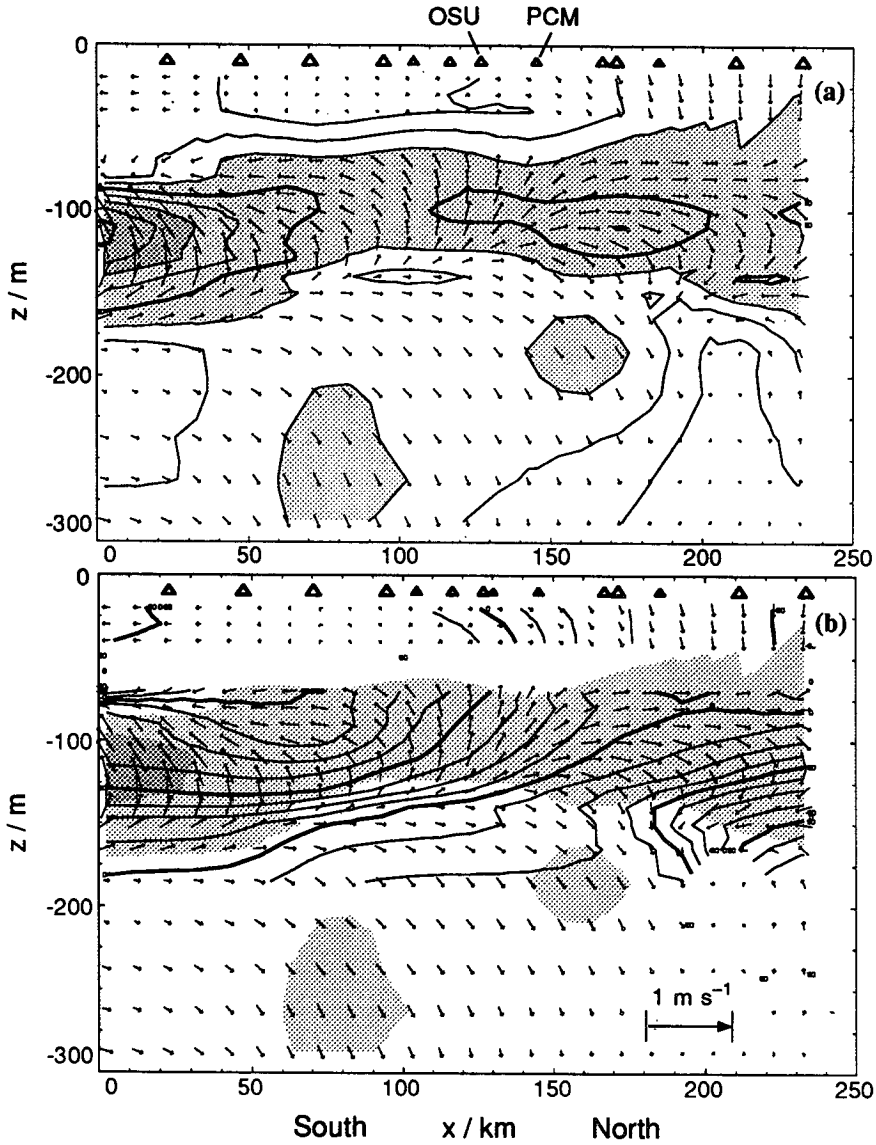

FIG. 19. Backrotated inertial vectors on day 298 interpolated to section A (see Fig. 2) in upper 300 m. Triangles show the projected location of all data within 20 km of the section. Moorings are labeled. The size of the triangle indicates the perpendicular distance. (a) Vectors with speed contours. Speeds greater than 0.15 m s^{-1} are shaded; contour interval: 0.05 m s^{-1}. (b) Vectors, shading from (a), and direction contours; contour interval: 22.5°.

$$\Theta_n(t) = \int_0^t \frac{c_n^2}{2f}\,\alpha(t)^2 dt. \qquad (16)$$

Gill (1984) then predicts that the amplitude of the mixed layer inertial currents will be reduced by a factor σ_n at time t_n such that $\Theta_n(t_n) = \frac{1}{2}\pi$. This formula may overpredict the decay rate if the region of strong inertial currents is much larger than the wavelength, as is certainly true near the end of our observations. Table 1 lists c_n and the cumulative σ_n. These were computed from a representative CTD profile, assuming a flat bottom and solving Gill's (1984) equations (3.3) and (3.4). The values of c_1 and c_2 are quite stable; using different CTD profiles results in total changes in their values of less than 10%. The values of σ_n depend both on the stratification and on the initial velocity profile assumed. The moored velocity data show a profile that decays to zero at 70 m. Using different CTD profiles and several shapes of velocity profiles all of which decay by 80-m depth leads to bounds of 0.093 to 0.15 for σ_1, 0.21 to 0.30 for σ_2, and 0.33 to 0.45 for $\sigma_1 + \sigma_2$.

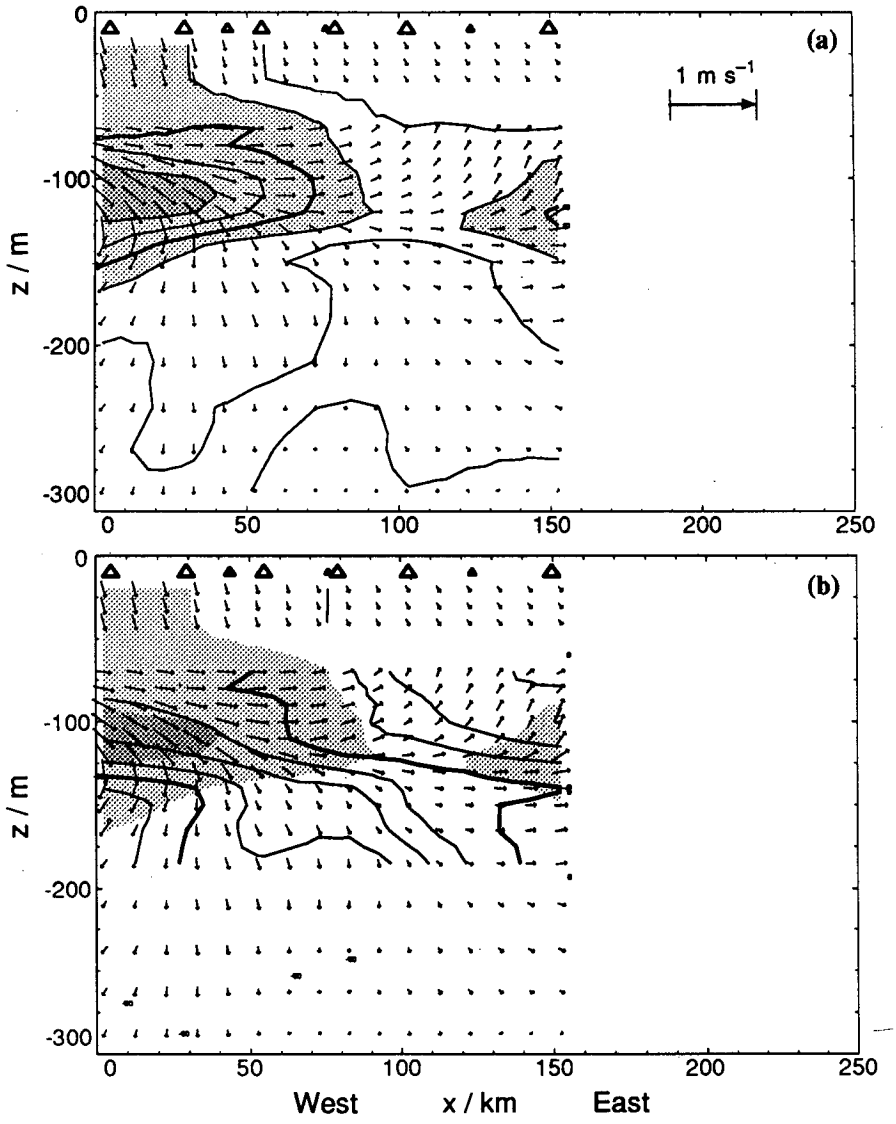

FIG. 20. Backrotated inertial vectors on day 298 interpolated to section B (see Fig. 2).

Figure 24 compares the observations and linear predictions of the quantity $\tau_{1/2}$, defined as the time for E_{fit} to fall to half its value on day 280 (day 282 for subgroup CL). Table 1 shows that $(1 - \sigma_1 - \frac{1}{2}\sigma_2)^2$ is close to 0.5, so the predicted $\tau_{1/2}$ corresponds to the time when mode 1 has separated and mode 2 is about halfway separated. We expect this to occur at approximately $\frac{1}{2}(t_1 + t_2)$, so we use a phase speed of $c_{1/2}^2 = \frac{1}{2}(c_1^2 + c_2^2) = (1.8 \text{ m s}^{-1})^2$ in (16). Observationally, we extract $\tau_{1/2}$ from Figs. 13–17. The 95% confidence limits are from the Monte Carlo simulated data. The observed and predicted $\tau_{1/2}$ are correlated, but the predicted values are about 2–5 days larger than the observed values; linear theory underpredicts the decay rate. Using $c_{1/2} = 2.5 \text{ m s}^{-1}$ gives a better fit (solid dots); this value is higher than can be justified from the CTD data.

Linear wave theory clearly fails at longer times. E_{tot} decays to 2.5% of its initial value by day 300, 23 days after the storm; E_{fit} decays to about 0.7% of its initial value. Using (16), we find that only modes 1–3 should have separated by this time, for any choice of CTD profile. Linear theory therefore predicts a reduction of E_{fit} to between $(1 - \sigma_1 - \sigma_2 - \sigma_3)^2$ and $(1 - \sigma_1 - \sigma_2 - \sigma_3 - \sigma_4)^2$ of its initial value. Depending on the stratification and velocity profile used, this yields a range of 9%–28%; this value is much larger than observed.

Gill's (1984) analysis may overestimate the decay rate for very large storms, since it assumes that the storm is smaller than the wavelength. Since the analysis

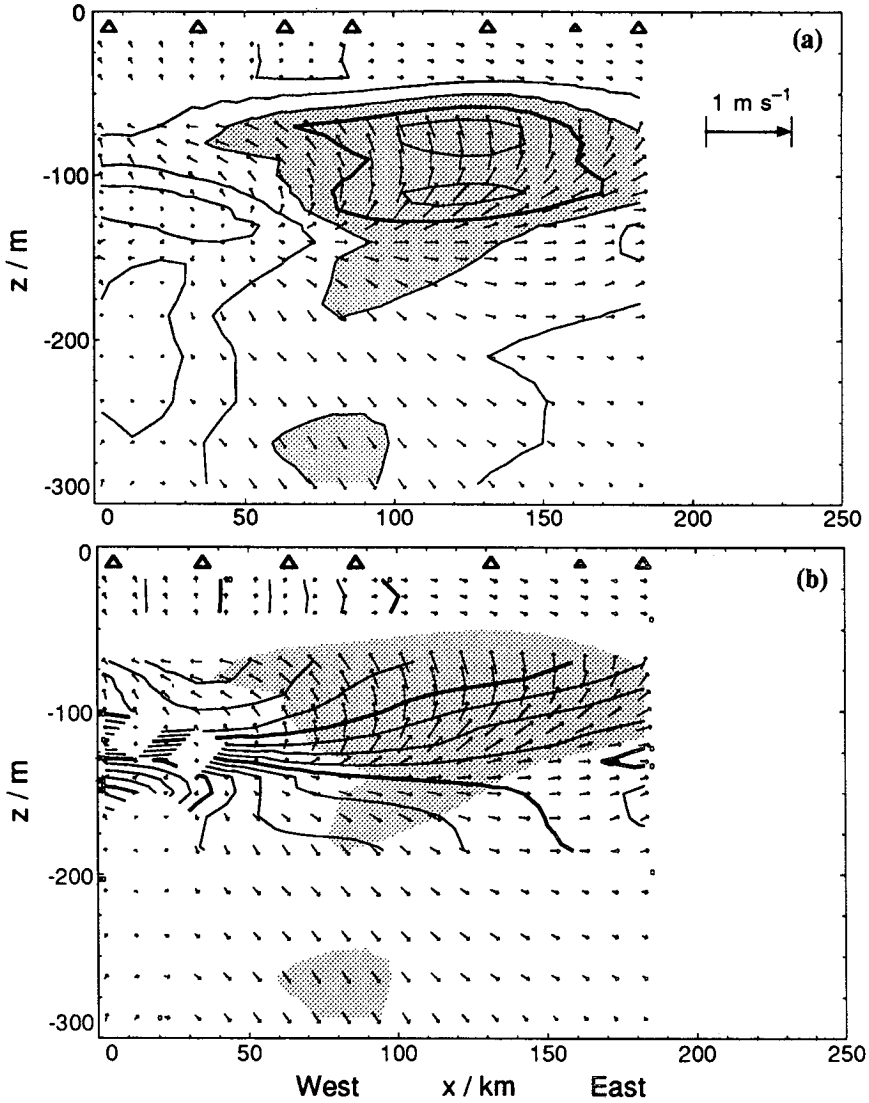

FIG. 21. Backrotated inertial vectors on day 298 interpolated to section C (see Fig. 2).

underpredicts the observed decay rate, including this effect will only strengthen our result.

Within the context of linear theory, the initial rate of decay of the mixed layer inertial currents is due to the separation and propagation of the low modes. Linear theory only slightly underpredicts the observations here. The final decay to background levels is due to the separation and propagation of the higher modes. Linear theory clearly requires that the high modes evolve more slowly than the low modes [Eq. (9)] and predicts that the final decay of mixed layer inertial currents to background levels will occur more slowly than the initial decay. Linear theory fails here, as the observed final decay occurs much more rapidly than predicted. The differences between the observations and the predictions of linear theory are therefore much greater for the high modes than for the low modes.

In Part II, a full numerical simulation confirms that Gill's analysis is an accurate approximation for this storm and that the storm size is not an important parameter.

e. Linear wave theory—Energy balance and horizontal propagation

We now compute the large-scale, depth-integrated inertial energy in the experimental region and compare its rate of change to that predicted by linear wave theory. We first estimate the inertial energy in the mixed layer immediately after the storm using plane-wave fits

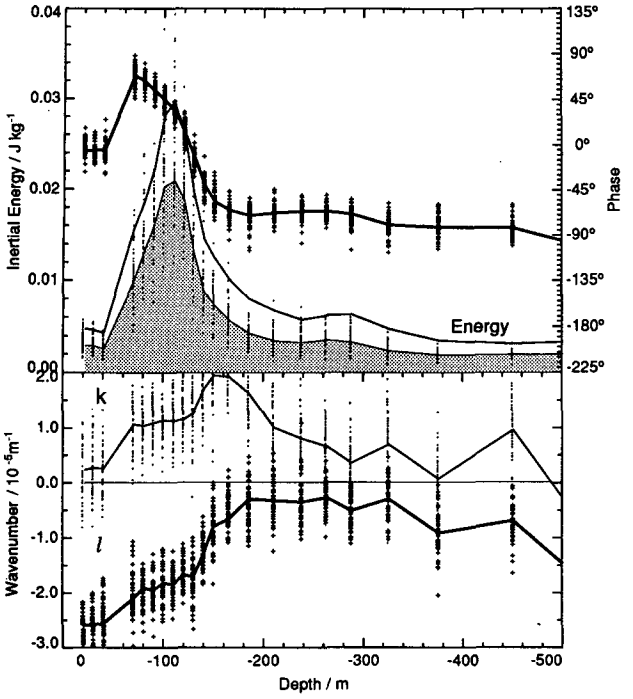

FIG. 22. Fit of (14) to backrotated inertial vectors on day 298. Fit parameters include the fit energy (top panel, shaded); the total energy (top panel, light line); the fit phase (top panel, heavy line); east–west wavenumber (k, bottom panel, light line); and north–south wavenumber (l, bottom panel, heavy line). The dots and pluses are the same parameters fit to 50 realizations of a Monte Carlo simulation of the data errors.

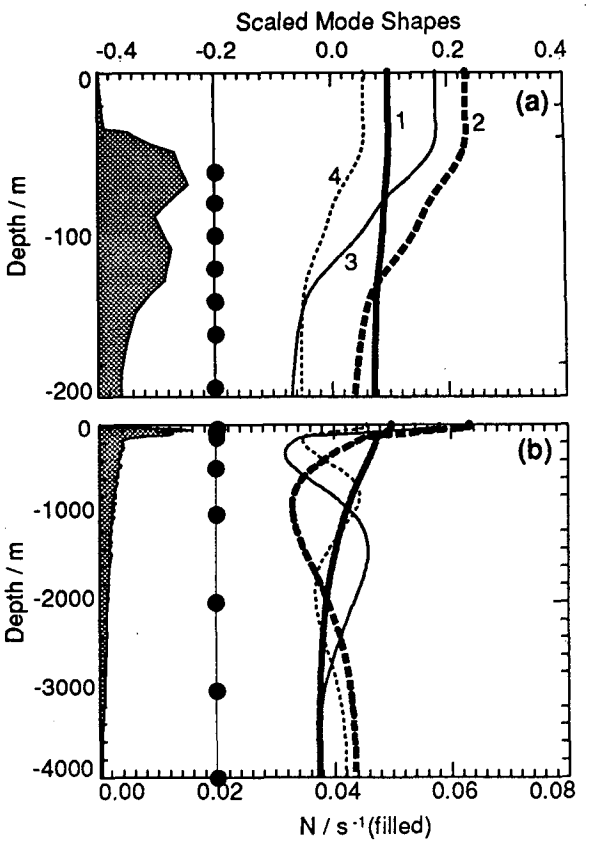

FIG. 23. Structure of first four baroclinic modes in upper 200 m (a) and entire water column (b). Profile of N^2 is shown on left. Modal amplitudes are normalized to σ_1 values in Table 1. Locations of OSU current meters are shown by the filled circles.

to the surface drifter data. For the entire array (Fig. 13), we find 0.15 ± 0.01 J kg^{-1}; for the "CL" region near the AXCP drops and moorings (Fig. 16), we find 0.16 ± 0.01 J kg^{-1}. The effective depth of these currents at the PCM mooring is 55 m; this implies a large-scale mixed layer inertial energy after the storm of $8.7 \pm 0.6 \times 10^3$ J m^{-2}.

On day 298, we use plane-wave fits to the AXCP data (Fig. 22). The energy density is $4.3 \pm 0.3 \times 10$ J m^{-2} in the upper 1000 m, of which 2.1×10^3 J m^{-2} (48%) is between 200 m and 1000 m. The energy density at the OSU mooring between 200 m and 1000 m averaged over days 295–301 is $2.0 \pm 0.3 \times 10^3$ J m^{-2}, which agrees well with the AXCP estimate. From 1000 m to the bottom, we have only the OSU mooring. The day 295–301 average energy density is $1.6 \pm 0.2 \times 10^3$ J m^{-2}. The depth-integrated energy density on day 298 is therefore $5.9 \pm 0.4 \times 10^3$ J m^{-2}.

A background level of inertial energy exists even without storm forcing. Using data from the OSU mooring before the storm, we estimate this as $1.2 \pm 0.3 \times 10^3$ J m^{-2}. Subtracting this, the inertial energy added to the water column by the storm is $7.5 \pm 0.7 \times 10^3$ J m^{-2}, and the amount remaining on day 298 is $4.7 \pm 0.5 \times 10^3$ J m^{-2}. The depth-integrated inertial energy decreases by 37% ± 10% in these 21 days.

In inviscid linear theory, energy can be lost from the experimental area only by horizontal propagation. Near-inertial waves cannot propagate northward as they are very close to the northward turning latitude

TABLE 1. Modal properties.

n	$\sum_{k=1}^{n} \sigma_k$	c_n (m s^{-1})	m (m^{-1})	$\sum_{k=1}^{n} E_k$ (J kg^{-1})	t_n (days)
1	0.098	2.28	0.007	0.011	10.9
2	0.330	1.24	0.012	0.037	16.4
3	0.510	0.89	0.017	0.057	20.4
4	0.566	0.65	0.023	0.063	25.0
5	0.602	0.51	0.030	0.067	29.7
6	0.651	0.41	0.037	0.073	34.1
7	0.718	0.35	0.043	0.080	37.6
8	0.773	0.31	0.048	0.086	40.6
9	0.791	0.28	0.055	0.087	44.1
10	0.798	0.25	0.062	0.088	47.7
15	0.856	0.16	0.095	0.094	63.6
20	0.907	0.12	0.126	0.098	77.1
25	0.927	0.09	0.158	0.100	89.6

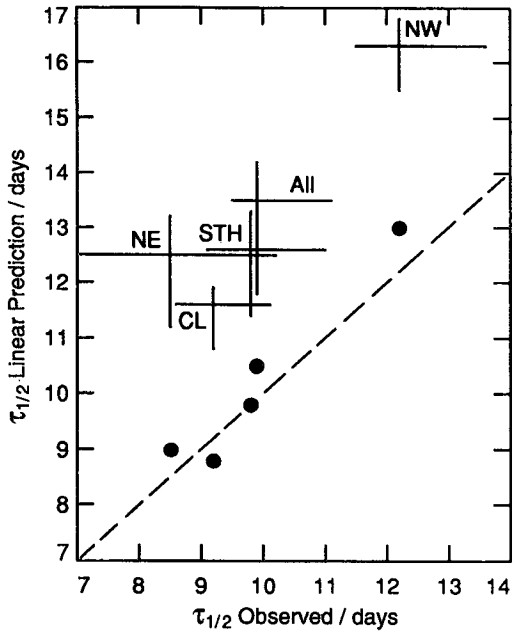

FIG. 24. Comparison of observed and predicted values of $\tau_{1/2}$, the time for the mixed layer inertial currents to decay to half their initial value. Confidence limits are approximately 95% and derived from 20 Monte Carlo simulations. Circles are predictions of $\tau_{1/2}$ when using an unrealistically high value of $c_{1/2} = 2.5$ m s^{-1}.

(Munk and Phillips 1968) and must therefore propagate southward. The horizontal group velocity of the nth vertical mode is given by (10). Propagation is in the direction of the horizontal wavenumber $\mathbf{k}$, which is toward the southeast quadrant both in the mixed layer (Figs. 13–17) and at depth (Fig. 22). The average southward propagation speed is computed from (10) using the average l between the time of the storm and day 298. This is about 1.0×10^{-5} m^{-1} (Fig. 13). During these 21 days, modes 1, 2, 3, and 4 are therefore predicted to have propagated 900 km, 265 km, 137 km, and 73 km, respectively, using the c_n in Table 1.

The storm on day 277 generated large inertial currents because its motion and structure conspired to rotate the wind stress clockwise at almost exactly the inertial frequency (Crawford and Large 1995; Large and Crawford 1995). The storm center passed about 500 km north of Ocean Storms. Much weaker inertial currents were probably generated north of the storm center, as the wind turned counterclockwise with time there. We estimate, therefore, that strong inertial currents were generated in a region that extended at most 500 km north of the Ocean Storms array. Mode 1 can clearly propagate out of this generation region in 21 days, while modes 2 and 3 can only partially do so. Using our values for σ, mode 1 carries 11%–17% of the total inertial energy, while modes 1 and 2 carry 33%–45%. If all of mode 1 and half of mode 2 propagate out of the generation region in 21 days, 23%–34% of the inertial energy is removed.

We make a second estimate by solving (4) exactly in a two-dimensional (north-depth) domain for each mode. At time $t = 0$ the energy in each mode has a Gaussian distribution with 75% of the energy in a band 750-km wide centered on 47.5°N. With time, the packet develops a north–south wavenumber βt and propagates southward. In 21 days modes 1, 2, 3, and 4 propagate 1400 km, 400 km, 230 km, and 120 km, respectively, and the fraction of the initial energy remaining at 47.5°N is 1.5%, 31%, 68%, and 89%, respectively. Using the computed values of σ_n, we find that 34%–46% of the initial energy at 47.5°N is lost by horizontal propagation.

Linear theory therefore predicts that horizontal propagation will remove most of the first mode energy, some of the energy in modes 2–4, and hardly any of the energy in the higher modes. The energy lost from the experimental area between the storm and day 298 is predicted to be between 23% and 46%. The major source of uncertainty is the distribution of energy between modes and the horizontal distribution of wind forcing. The data indicate that 37% ± 10% of the energy was actually lost. These agree to within the errors.

f. Linear theory—shear

Figure 11 shows a large decrease in upper ocean shear over these same 21 days. The low modes contribute little to the shear profile; the higher modes, which do contribute, propagate little in 21 days. The decrease in shear, therefore, is not explained by linear theory.

9. Summary

A strong, isolated storm generated strong inertial currents in the upper ocean. We follow the evolution of these inertial currents for nearly a month after the storm. Major results are as follows.

a. Subinertial currents

The array was intentionally located in a region of weak flow, so that wind forced effects would be easy to measure:

- The subinertial flow was dominated by low-mode, nondivergent geostrophic motions with a level of no motion near 800 m.
- The spatial mean currents were northeastward at 0.025 m s^{-1}. The eddy currents were 0.05 m s^{-1} rms, of dominantly anticyclonic vorticity (0.023f rms), and a wavelength of roughly 100 km.
- Water parcels move through the nearly stationary eddy field much faster than it evolves, so absolute vorticity is conserved along streamlines to the measurement accuracy.

b. Inertial frequency currents

- The storm produced energetic (0.35–0.7 m s^{-1}) inertial motions in the mixed layer. Their magnitude can be predicted from the measured winds as interpreted by Large et al. (1995).
- The horizontal structure of the inertial currents in the upper 200 m can be accurately described by a single, time-dependent horizontal wavenumber.
- The initial horizontal wavelength of the inertial currents was large, about 1700 km. This is about 50% larger than would be predicted by assuming that a storm of fixed shape advected over the region at the observed rate.
- The east–west wavenumber of the inertial currents remains constant after the storm, while the north–south wavenumber decreases at about $-\beta t$ as expected for inertial currents on a β-plane.
- Mixed layer inertial energy decayed to half of its initial value in 8–14 days, depending on location, and to background levels in 20–25 days.
- Total water column inertial energy decreased by 37 ± 10% in 21 days.
- Inertial currents propagated downward out of the mixed layer. Immediately after the storm, they extended 20–30 m below the mixed layer. They spread about 20 m deeper in the following 10 days. More rapid vertical propagation followed in the next 10 days, with a detectable increase in inertial energy extending throughout the water column. A maximum in inertial energy was formed at about 100 m (the Beam) and persisted for the next 10 days.
- The rapid transfer of energy from the mixed layer starting about 10 days after the storm was accompanied by a clockwise turning of the inertial frequency velocity vector with depth and a slightly superinertial frequency.
- Although most of the inertial frequency energy followed the large-scale pattern described above, smaller-scale deviations from this pattern were present.
- The shear at the base of the mixed layer decreased by a factor of ~4 as the inertial energy propagated vertically.

The observed evolution of the inertial currents can only partially be described by the linear internal wave equations. Specifically:

- The increase in north–south wavenumber at a rate $-\beta$ is accurately predicted by linear theory.
- The decrease in total water column inertial energy is explained by the propagation of the lowest few baroclinic modes out of the generation region to within the large (40%) experimental errors.
- Energy loss from the mixed layer occurs only when the horizontal wavenumber of the inertial currents becomes sufficiently large and is accompanied by a superinertial frequency and a clockwise rotation of velocity with depth. The energy loss occurs more rapidly in regions with a larger horizontal wavenumber. All these features are qualitatively consistent with linear theory.
- Linear theory underpredicts the initial rate at which inertial energy is lost from the mixed layer by 20–50%, underestimating the time for half the energy to be removed by 2–4 days. The difference significantly exceeds the measurement error (1 day).
- The decay of the mixed layer inertial energy to background levels and the decrease of the shear below the mixed layer occur much more rapidly than is predicted by linear theory.

10. Discussion

The main result of this paper is that the linear theory of near-inertial frequency waves propagating in a uniform background can only partially explain our observations. The agreement between the theory and observations is best for those quantities that are dominated by low modes, that is, the total energy and the general vertical structure, and are worst for those quantities that are dominated by the high modes, that is, the final decay of the mixed layer energy and the shear level. Thus, although the data are insufficient to do an accurate modal decomposition, they indicate that linear theory is accurate only for the lowest modes.

The failure of simple linear theory is perhaps not very surprising. The ocean in which the waves propagate is not homogeneous nor are the equations of motion strictly linear. Energy can be lost from inertial motions by nonlinear interactions with other types of motions. Parts II and III of this paper investigate these issues.

Practically, our data demonstrate the important role of horizontal scale in controlling the residence time of mixed layer near-inertial motions. For the case studied here, the storm produced inertial currents of such large horizontal scale that little propagation initially occurred. The largest inhomogeneity in the ocean was β, so this controlled the horizontal scale of the inertial currents. In general, however, small-scale inertial currents can be generated by the wind or created by the mesoscale eddy field (Klein and Treguier 1993). Gill (1984) suggests replacing $-rU$ in (1) by

$$-c_1^2\sigma_1/(\pi f)\nabla^2 U$$

as a way of including the effect of horizontal scale in simple models of the mixed layer. This has the effect of making the mixed layer inertial currents and the shear at the mixed layer base decay at the same rate as the first mode. Our observations are consistent with this idea since the observed mixed layer inertial energy and shear decay at low mode rates even at long times. However, until we know why linear theory underpredicted these decay rates, the widespread use of such a parameterization is premature.

Acknowledgments. Russ Davis generously provided the wind and near-surface ADCP data. EAD thanks Brad Bell for help with programming. Eric Kunze made many helpful comments on an early draft of this article. Comments by the reviewers were invaluable. This work was supported by the Office of Naval Research under Contracts N00014-84-C-0111 and N00014-87-K-0004, and Grant N00014-90-J-1104.

APPENDIX

Details of Data Analysis

a. Drifter interpolation by objective analysis

We interpolate the irregularly spaced time series of drifter positions assuming that these positions are realizations of an isotropic, stationary random process with known statistics using the objective analysis techniques outlined by McIntosh (1990) and Davis et al. (1992). The assumption of a stationary signal will later be relaxed to allow for slowly changing statistics to accommodate nonstationarity of the variance of the low-frequency and higher-frequency components of the dataset.

The positions of the drifters at time i are estimated using N observations at times t_n according to

$$\bar{\mathbf{x}}(t) = \sum_{n=1}^{N} [\alpha_n(t)\mathbf{r}_n + \gamma_n(t)\mathbf{z} \times \mathbf{r}_n], \quad \text{(A1)}$$

where $\bar{\mathbf{x}}(t)$ is the estimate of the float position at time t, $\mathbf{r}_n$ is the observed position at time t_n, and $\mathbf{z}$ is the vertical unit vector. In this formula α takes into account how longitude observations are used in estimating the longitude component of the position and how latitude observations are used in estimating the latitude component. Similarly, γ takes into account how the latitude observations influence the estimated longitude estimate and how the longitude observations influence the latitude estimate. This means that rotary tendencies like inertial or tidal motions can be modeled accurately. These weights are calculated by minimizing the mean-square position error, $\epsilon = \langle|\bar{\mathbf{x}}(t) - \mathbf{x}(t)|^2\rangle$, subject to

$$\sum_{n=1}^{N} \alpha_n = 1 \quad \text{(A2)}$$

and

$$\sum_{n=1}^{N} \gamma_n = 0. \quad \text{(A3)}$$

These constraints are necessary to assure that the observed mean and the estimated mean are similar. The positions could be referenced to the sample mean, but this would make the time series nonstationary.

The analysis also requires knowledge about the covariance function and the distribution function of the error. The error will be modeled as Gaussian, uncorrelated with the data, with zero mean and a position variance of 500 m^2. Since the observed spectra of position have a large inertial peak and a red low-frequency spectrum, we use correlation functions that mimic these features. The correlation functions required for minimizing the mean squared position error are

$$\langle x(t_1)x(t_2)\rangle = \hat{U}^2\tau_L^2 e^{-(t_1-t_2)^2/2\tau_L^2} + \hat{u}^2 \frac{\tau_I^2}{f_0^2\tau_I^2 + 1} \cos(f_0(t_2 - t_1))e^{-(t_1-t_2)^2/2\tau_I^2} \quad \text{(A4)}$$

and

$$\langle x(t_1)y(t_2)\rangle = \hat{u}^2 \frac{\tau_I^2}{f_0^2\tau_I^2 + 1} \sin(-f_0(t_2 - t_1))e^{-(t_1-t_2)/2\tau_I^2}, \quad \text{(A5)}$$

where $\hat{U}^2$ is the variance of the low-frequency component of the velocity and $\hat{u}^2$ is the variance of the inertial component of the velocity. These variances are computed using a moving average of 40 points for the inertial component and 80 points for the low-frequency component. We use $\tau_L = 3$ days and $\tau_I = 4/f_0$. As described in the text, these values give inertial and subinertial currents very close to those estimated by D'Asaro (1992) for this same dataset.

b. Mapping the subinertial velocity

We map the subinertial velocity field as described by Bretherton et al. (1976) using the analytical correlation function from McWilliams (1976a,b). Figure A1 shows estimates of the transverse (Fig. A1a) and longitudinal (Fig. A1b) correlation functions for all subinertial drifter velocities in Fig. 5a. Using all possible buoy pairs produces a longitudinal correlation function (asterisks) with a minimum in coherence at 5 km. This seems anomalous. Many of the data pairs with short spatial lags are really autocorrelation pairs for buoys with small speed; these are the data most likely to be decorrelated by wind-forced currents. Removing buoys with speeds less than 0.04 m s^{-1} reduces the anomalously low correlations at 5 km (pluses) but has little effect at larger lags. A purely spatial correlation function was constructed by computing the lagged covariances for each day and averaging the 21 covariances at each lag to form a correlation function (squares in Fig. A1). Far fewer pairs are used, so the correlation function is much noisier and 20 km bins are required. The two data sampling schemes produce significantly different transverse correlation functions. A fit of the McWilliams (1976a,b) analytical correlation functions (solid lines in figure) with a longitudinal correlation scale of 150 km and a transverse scale of 40 km yields a good fit to the longitudinal data, but it overestimates the negative lobe of the transverse correlation function. This discrepancy cannot be corrected by varying the coefficients; it indicates that the objectively analyzed

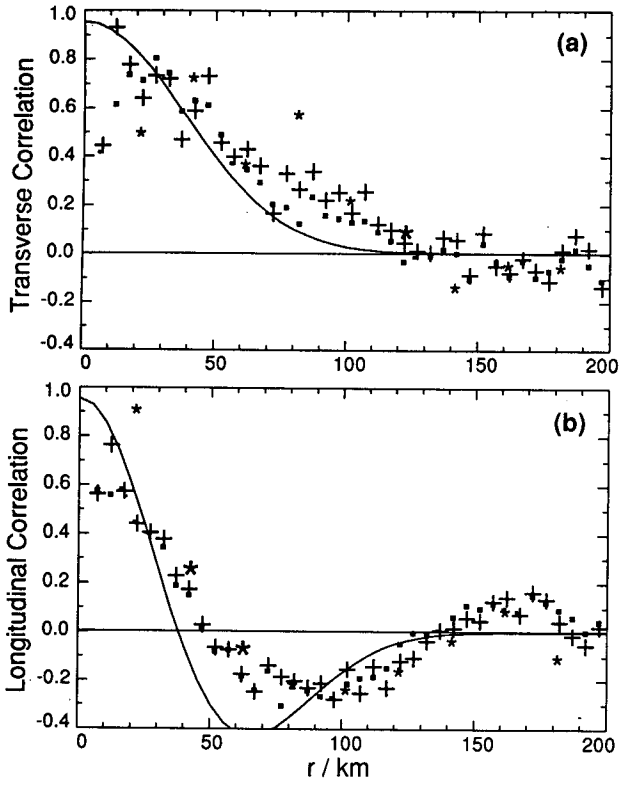

FIG. A1. Estimated correlation functions for subinertial velocity data in Fig. 2. (a) Transverse and (b) longitudinal. Symbols indicate type of averaging: asterisks: all data grouped in 5-km bins; pluses: data with a speed greater than 0.04 m s^{-1} grouped in 5-km bins; and squares: data from each day averaged in 20 km bins and these covariances, are averaged to form correlations; lines: correlation functions used in analysis.

fields using this correlation function may have some systematic errors. Objective analysis also requires an estimate of the small-scale "noise" in the field due to instrumental error and small-scale oceanographic motions. Instrumental, windage, and demodulation errors for the drifters are estimated at 0.01 m s^{-1} in each component, or about 5% of the variance. The fields produced using these parameters differ from those produced using two-dimensional quadratic smoothing splines (Wahba 1975) by less than the estimated error.

Objective analysis of the dynamic height data (Fig. 3) used a correlation function of the form $e^{-(r/\Delta)^2}$ for separation r. Using Δ = 100 km gives a rough fit to the correlation function estimated from the data. Again, smoothing splines produce a very similar field.

c. *Fitting (14)*

For each value of the parameters k and l, U_{fit} is determined by linear least squares. A dense search in k, l space is used to find a starting point for a nonlinear, least squares minimization using an algorithm similar to that of Marquardt (1963).

d. *Monte Carlo simulation*

We model the field of inertial currents by (14) using the fit values of U_{fit}, k, and l and consider U_R to be a continuous random function characterized by its correlation function. Figure A2 shows the covariance function of the measured U_R (dashed) computed for all fits between days 276 and 300. Realizations of U_R were generated by smoothing an array of random Gaussian vectors with a two-dimensional quadratic smoothing spline (Craven and Wahba 1979), fitting this field with (15), and computing the residual from this fit. The variance and amount of smoothing were chosen so that the correlation function of the data is the same as that of these realizations within their confidence limits (solid line, Fig. A2). Note that U_R is spatially inhomogeneous since (15) fits data better near the center of the array than near its edge. The simulated U_R simulate this inhomogeneity well except for the northwest corner of the domain where the simulated variance is less than that of the data. Adjusting the simulated fields to improve this does not make a significant difference in the confidence limits computed from the simulations, and we did not include such an adjustment.

e. *Fit of wavenumbers to AXCP data*

The parameters of the wavenumber fit to the AXCP data (Fig. 22) are determined as described in (c) above. Their errors are determined by a Monte Carlo simulation. The fitting procedure is simulated by generating realizations of U_R with a correlation function similar to that found for the real U_R. Figure A3 shows the correlation function averaged over data from 55 to 175 m

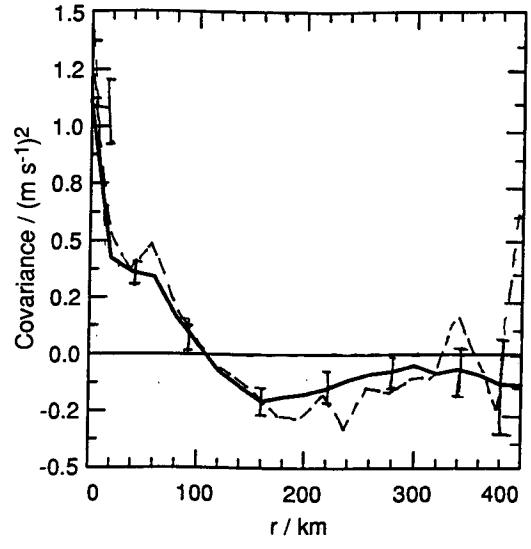

FIG. A2. Estimated covariance functions for U_R in (15) from the data (dashed line) and from an average of 20 Monte Carlo simulations of the data (solid line). The error bars represent approximately 95% confidence limits determined from these simulations.

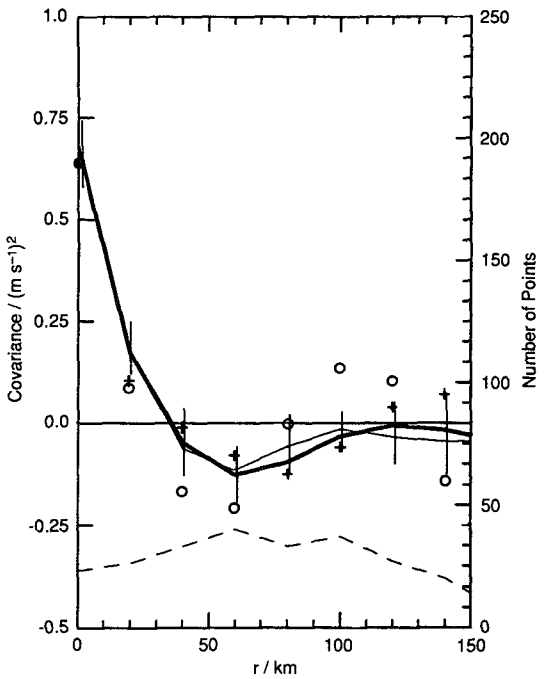

FIG. A3. Lagged longitudinal (heavy line, O) and transverse (light line, +) for fit residual averaged from 55 m to 175 m. Symbols are for data; lines and 95% confidence limits are derived from the Monte Carlo simulation.

(circles). This is simulated by generating a field of complex Gaussian random numbers with expected variance at each depth determined by $|U_R|^2$ computed from the fit of (15). These are then smoothed with splines (Craven and Wahba 1979) with a smoothing parameter of 1000 m to generate synthetic realizations of U_R. The correlation function of these realizations is close to that of the data in the 55–175-m depth range (Fig. A3). These U_R are used to generate synthetic data which are then fit to form Monte Carlo realizations of the data. The variance of U_R appears to be spatially variable, but not so much that it could not be a realization of this model.

REFERENCES

Bell, T. H., 1978: Radiation damping of inertial oscillations in the upper ocean. *J. Fluid Mech.*, **88,** 289–308.

Bretherton, F. P., R. E. Davis, and C. B. Fandry, 1976: A technique for objective analysis and design of oceanographic experiments applied to MODE-73. *Deep-Sea Res.*, **23,** 559–582.

Craven, P., and G. Wahba, 1979: Smoothing noisy data with spline functions: Estimating the correct degree of smoothing by the method of generalized cross validation. *Numer. Math.*, **3,** 377–403.

Crawford, G. B., and W. G. Large, 1995: A numerical investigation of resonant inertial response of the ocean to wind forcing. *J. Phys. Oceanogr.*, submitted.

D'Asaro, E. A., 1985: The energy flux from the wind to near-inertial motions in the surface mixed layer. *J. Phys. Oceanogr.*, **15,** 1043–1059.

——, 1989: The decay of wind-forced mixed layer inertial oscillations due to the β effect. *J. Geophys. Res.*, **94,** 2045–2056.

——, 1992: Estimation of velocity from Argos-tracked surface drifters during OCEAN STORMS. *J. Atmos. Oceanic Technol.*, **9,** 680–686.

——, 1995a: Upper-ocean inertial currents forced by a strong storm. Part II: Modeling. *J. Phys. Oceanogr.*, **25,** 2937–2952.

——, 1995b: Upper-ocean inertial currents forced by a strong storm. Part III: Interaction of inertial currents and mesoscale eddies. *J. Phys. Oceanogr.*, **25,** 2953–2958.

——, and H. T. Perkins, 1984: A near-inertial internal wave spectrum for the Sargasso Sea in late summer. *J. Phys. Oceanogr.*, **14,** 489–505.

——, T. B. Sanford, R. G. Drever, M. D. Morehead, and G. L. Welsh, 1990: Air expendable current profiling during the OCEAN STORMS experiment. APL-UW TR 8916, Applied Physics Laboratory, University of Washington, Seattle, WA, 66 pp.

——, and M. D. Morehead, 1991: Internal waves and velocity fine structure in the Arctic Ocean. *J. Geophys. Res.*, **96,** 12 725–12 738.

Davis, R. E., R. A. de Szoeke, and P. P. Niiler, 1981: Variability in the upper ocean during MILE. Part II: Modeling the mixed layer response. *Deep-Sea Res.*, **28,** 1453–1475.

——, D. C. Webb, L. A. Regier, and J. Dufour, 1992: The autonomous Lagrangian circulation explorer (ALACE). *J. Atmos. Oceanic Technol.*, **9,** 264–285.

Ekman, V. W., 1905: On the influence of the earth's rotation on ocean currents. *Ark. Mat. Astron. Fys.*, **2**(11), 1–53.

Eriksen, C. C., 1988: On wind forcing and observed oceanic wave number spectra. *J. Geophys. Res.*, **93,** 4985–4992.

Gill, A. E., 1984: On the behavior of internal waves in the wakes of storms. *J. Phys. Oceanogr.*, **14,** 1129–1151.

Horgan, M. S., R. G. Drever, and M. A. Kennelly, 1989: XCP phase and gain tests. APL-UW TR 8924, Applied Physics Laboratory, University of Washington, Seattle, WA, 72 pp.

Käse, R. H., 1979: Calculations of the energy transfer by the wind to near-inertial internal waves. *Deep-Sea Res.*, **26,** 227–232.

Klein, P., and A. M. Treguier, 1993: Inertial resonance induced by an oceanic jet. *J. Phys. Oceanogr.*, **23,** 1897–1915.

Kroll, J., 1982: An unstable uniform slab model of the mixed layer as a source of downward propagating near-inertial motion. Part I: Steady mean flow. *J. Mar. Res.*, **40,** 1013–1033.

Kundu, P. K., and R. E. Thomson, 1985: Inertial oscillations due to a moving front. *J. Phys. Oceanogr.*, **15,** 1076–1084.

Kunze, E., 1985: Near-inertial wave propagation in geostrophic shear. *J. Phys. Oceanogr.*, **15,** 544–565.

Large, W. G., and S. Pond, 1981: Open ocean momentum flux measurements in moderate to strong winds. *J. Phys. Oceanogr.*, **11,** 324–336.

——, and G. B. Crawford, 1995: Observations and simulations of upper-ocean response to wind events during the Ocean Storms Experiment. *J. Phys. Oceanogr.*, **25,** 2831–2852.

——, J. Morzel, and G. B. Crawford, 1995: Accounting for surface wave distortion of the marine wind profile in low-level Ocean Storms wind measurements. *J. Phys. Oceanogr.*, **25,** 2959–2971.

Leaman, K. D., 1976: Observations on the vertical polarization and energy flux of near-inertial waves. *J. Phys. Oceanogr.*, **6,** 894–908.

Levine, M. D., and V. Zervakis, 1995: Near-inertial wave propagation into the pycnocline during Ocean Storms: Observations and model comparison. *J. Phys. Oceanogr.*, **25,** 2890–2908.

Marquardt, D. W., 1963: An algorithm for least-squares estimation of nonlinear parameters. *J. Soc. Indus. Appl. Math.*, **11,** 431–440.

Matear, R. J., 1993: Circulation within the Ocean Storms area located in the northeast Pacific Ocean determined by inverse methods. *J. Phys. Oceanogr.*, **23,** 648–658.

McIntosh, P. C., 1990: Oceanographic data interpolation: Objective analysis and splines. *J. Geophys. Res.*, **95,** 13 529–13 541.

McWilliams, J. C., 1976a: Maps from the Mid-Ocean Dynamics Experiment. Part I: Geostrophic streamfunction. *J. Phys. Oceanogr.*, **6,** 810–827.

——, 1976b: Maps from the Mid-Ocean Dynamics Experiment. Part II: Potential vorticity and its conservation. *J. Phys. Oceanogr.*, **6,** 828–846.

Müller, P., D. J. Olbers, and J. Willebrand, 1983: The IWEX spectrum. *J. Geophys. Res.*, **83,** 479–500.

Munk, W., and N. Phillips, 1968: Coherence and band structure of inertial motion in the sea. *Rev. Geophys.*, **6,** 447–472.

Niiler, P. P., and J. D. Paduan, 1995: Wind-driven motions in the northeast Pacific as measured by Lagrangian drifters. *J. Phys. Oceanogr.*, **25,** 2819–2830.

——, R. E. Davis, and H. J. White, 1987: Water-following characteristics of a mixed layer drifter. *Deep-Sea Res.*, **34,** 1867–1881.

Paduan, J. D., and P. P. Niiler, 1993: Structure of velocity and temperature in the northeast Pacific as measured with Lagrangian drifters in fall 1987. *J. Phys. Oceanogr.*, **23,** 585–600.

——, R. A. de Szoeke, and R. A. Weller, 1989: Inertial oscillations in the upper ocean during the Mixed Layer Dynamics Experiment (MILDEX). *J. Geophys. Res.*, **94,** 4835–4842.

Pollard, R. T., 1970: On the generation by winds of inertial waves in the ocean. *Deep-Sea Res.*, **17,** 795–812.

——, 1980: Properties of near-surface inertial oscillations. *J. Phys. Oceanogr.*, **10,** 385–398.

——, and R. C. Millard Jr., 1970: Comparison between observed and simulated wind-generated inertial oscillations. *Deep-Sea Res.*, **17,** 813–821.

Price, J. F., 1981: Upper ocean response to a hurricane. *J. Phys. Oceanogr.*, **11,** 153–175.

——, 1983: Internal wave wake of a moving storm. Part I: Scales, energy budget and observations. *J. Phys. Oceanogr.*, **13,** 949–965.

——, R. A. Weller, and R. Pinkel, 1986: Diurnal cycling: Observations and models of the upper ocean response to diurnal heating, cooling and wind mixing. *J. Geophys. Res.*, **91,** 8411–8427.

——, ——, and R. R. Schudlich, 1989: Wind driven ocean currents and Ekman transport. *Science,* **238,** 1534–1538.

Qi, H., R. A. de Szoeke, C. A. Paulson, and C. C. Eriksen, 1995: The structure of near-inertial waves during Ocean Storms. *J. Phys. Oceanogr.*, **25,** 2853–2871.

Sanford, T. B., P. G. Black, J. R. Haustein, J. W. Feeney, G. Z. Forristall, and J. F. Price, 1987: Ocean response to a hurricane. Part I: Observations. *J. Phys. Oceanogr.*, **17,** 2065–2083.

——, R. G. Drever, J. H. Dunlap, and E. A. D'Asaro, 1982: Design, operation and performance of an expendable temperature and velocity profiler (XTVP). APL-UW 8110, Applied Physics Laboratory, University of Washington, Seattle, WA, 83 pp.

Shen, C., and J. McWilliams, 1978: Optimal arrays for estimating potential derivatives and non-linear terms in a potential vorticity budget. Special Report No. 85, Department of Oceanography, University of Washington, Seattle, WA, 46 pp.

Smith, R., 1973: Evolution of inertial frequency oscillations. *J. Fluid Mech.*, **60,** 383–389.

Tabata, S., L. A. F. Spearing, R. H. Bigham, B. G. Minkley, J. Love, D. Yelland, J. Linguanti, and P. M. Kimber, 1988: STP/hydrographic observations along line P, Station P, Line R and associated lines, and in the "OCEAN STORMS" area. Canadian Data Report of Hydrography and Ocean Sciences, No. 70, 132 pp. [Available from Institute of Ocean Sciences and Department of Fisheries and Oceans, Sidney, BC, Canada.]

Thomson, R. E., and W. S. Huggett, 1981: Wind-driven inertial oscillations of large spatial coherence. *Atmos.–Oceans,* **19,** 281–306.

Wahba, G., 1975: Smoothing noisy data with spline functions. *Numer. Math.*, **24,** 383–393.

Webster, F., 1968: Observation of inertial-period motions in the deep sea. *Rev. Geophys.*, **6,** 473–490.

Zervakis, V., and M. D. Levine, 1995: Near-inertial energy propagation from the mixed-layer: Theoretical considerations. *J. Phys. Oceanogr.*, **25,** 2872–2889.